Processes involved in the propagation of rifts near Hemmen Ice Rise in the Ronne Ice Shelf, Antarctica.

Eric Larour*, Eric Rignot*, and Denis Aubry**

* *Jet Propulsion Laboratory, California Institute of Technology, Pasadena 91109, California, U.S.A.*

** *Laboratoire de Mecanique des Sols, Structures et Materiaux, Ecole Centrale Paris, Paris, France*

ABSTRACT

We use radar interferometric images collected by ERS-1 and Radarsat-1 to observe the rupture tip of rifts along Hemmen Ice Rise on the Ronne Ice Shelf, Antarctica. Interferograms generated in 1992 and 1997 allow us to observe the deformation of ice accumulated over respectively 9 and 24 days. We combine these interferograms together to separate the continuous process of creep deformation from the more cyclic motion caused by variations in ocean tides. Then, we confront the observations with a deformation model for ice and obtain the following results: 1) The tidal oscillation of the Ronne Ice Shelf only yields small deformations near the tip of rifts. 2) Along the rifts, the icefront and at the rupture tips, vertical creep is observed and well explained by a model of viscous deformation of ice. Furthermore, the deformation pattern observed around the rupture tips can be used to determine whether the rift propagation is active or blocked. 3) The deformation pattern predicted by linear elastic fracture mechanics is too weak compared to the viscous adjustment of the ice, to be observed, but the propagation rate of the rifts is well explained by linear elastic fracture mechanics. These results are an important step towards developing a better model of ice-shelf calving mechanism.

1 Introduction

Iceberg calving plays a key role in the evolution of ice shelves. It controls a large fraction of the ice discharge into ocean (Jacobs and others (1992)) and involves important processes, for example the formation and propagation of rifts, which influence the mechanical stability of ice shelves (Doake and others 1998).

A good understanding of the mechanisms involved in the calving process is therefore necessary. Some of the main unknown characteristics of iceberg calving are the timing of calving events, the origin of the breakup of tabular icebergs, the origin of the rifts that give birth to giant icebergs, the mode and rate of propagation of the rifts, and what controls them.

All these factors are important to establish a calving law which will allow a model of calving mechanisms on an ice shelf. In this article, we focus our attention on the eastern sector of the Ronne Ice Shelf. On October 13^{th} of 1998, in the zone surrounding Hemmen Ice Rise near Berkner Island, a tabular iceberg of 145x50 km^2 in size broke off from the ice shelf. This was one of the largest calving events ever witnessed in Antarctica. The fact that it originated from a prexisting rift which was part of a larger field of rifts around Hemmen Ice Rise, with satelite imagery (INSAR) collected before and after, makes it an ideal event to study calving mechanisms.

In this article, we use radar images covering a period of 6 years before the final breakup. These radar images are processed interferometrically in order to obtain both the horizontal and vertical velocity of the ice shelf. We also use the amplitude imagery to measure the propagation rate of the rifts emmanating from Hemmen Ice Rise and the evolution of the geometry of those rifts. We analyse this information to understand the ice shelf evolution prior to calving.

The discussion presents a series of results. First, we show that the process associated with the tidal motion of the Ronne Ice Shelf influence very little the propagation of rifts and that the main contribution to their propagation comes from the horizontal flow of the ice shelf. Then we present an explanation of the origin of the deformation pattern observed near the rift tips with INSAR using

a viscous model of ice. We use these patterns to characterize the fracturing process. We show that the stress distribution around the tip of the rifts is too weak to be observed with an interferogram, and masked by the viscous adjustment of the ice-shelf to the propagation of the rupture. We measure propagation rates of the Ronne Ice Shelf rifts with predictions for linear elastic fracture mechanics. We conclude by discussing how these results will help develop a better modelization of fracture processes on an ice-shelf.

2 Study area

Hemmen Ice Rise, Ronne Ice Shelf, lays on the eastern flank of Berkner Island (Figure 1a). This ice rise is at the origin of a vast field of rifts, some having a length of up to 40 km. Crevasses originating from the shear margin of the ice rise, transform into rifts and propagate parallel to the ice front at rates about 1000 ma^{-1}, which is comparable to the ice shelf velocity. On October 13^{th} 1998, the rift marked number 3 on Figure 1a became unstable and broke off, giving birth to tabular iceberg A 38 of 145 km in length.

The complex pattern of ice motion around HIR prior to calving was discussed in details by Rignot and Mc Ayeal (1998). The ice shelf flows with a decreasing velocity along the flanks of Berkner Island, and there is a general rotation of the ice shelf around Berkner Island towards the east. Yet the presence of the rise as an anchor to the ice shelf, and the formation of ice melange between the rifts,are at the origin of a counter rotation: in Figure 1a, rifts 1 and 2 which are still attached to Hemmen Ice Rise rotate eastwards, but rifts 3,4 and 5, which are free from the rise, rotate towards the west. This rotation is at the origin of the opening of crevasses which form rifts and propagate parallel to the ice front.

3 Observations

We use interferograms built from ERS-1 and 2 and Radarsat-1 radar satellites at two different epochs, 1992 and 1997, prior to the event of 1998. These interferograms allow us to observe the de-

formation of ice accumulated over respectively 9 and 24 days. We combine these interferograms in different ways to separate the continuous process of creep deformation from the more cyclic motion due to ocean tides. We also use the radar images to evaluate changes in geometry, and propagation rate of the rift. Table 1 summarises the images we used and the combinations we made.

3.1 Geometrical observations

From the amplitude images in 1992, 1996, 1997 and 1998, we measure the propagation rates of the opening rifts. The radar amplitude images are geocoded at a sample spacing of 50 m on a polar stereographic grid. We measure the difference in length of the rifts, between the four radar images, by detecting characteristic features along the rifts which are common between images. We give the results in Table 2.

It can be seen that rifts 4 and 5 are basically inactive. In fact, the rates given in Table 2 are more or less at the noise level. This observation is confirmed by the fact that the imprints of rifts 4 and 5 were still visible on iceberg A38 (Figure 2b). This inactivity may be due to the sea ice filling the rifts or to the deconnection from HIR. The nearer the icefront, the thicker is this layer of ice, which gives cohesion to the flanks of the rift, as demonstrated by Rignot and Mac Ayeal (98). Also, the lateral shear is less important far from HIR, which makes it harder for the rifts to propagate.

Rifts 1,2 and 3 are the most active. Rifts 2 and 3 show a similar pattern of propagation. If we make the assumption that the propagation is continuous, we find that rifts 2 and 3 decelerated between 92 and 97, and accelerated suddenly in 3 months at the beginning of 98. The final rupture of rift 3 took place on October 1998, 7 months later. Rift 1 did not propagate during 4 years between 92 and 96, but started to propagate again at high velocity in 1997. This is consistent with the position of rift 1 along the ice rise margins: it is located (Figure 1a and 2a) at a point where the bay sides diverge. Sanderson (79) has shown that at this point, the strain rate reaches a maximum, therefore facilitating a sudden propagation of rifts, and ice-shelf calving.

3.2 Dynamics of the ice shelf

We use interferograms to characterize the ice shelf dynamics. Different combinations of interferograms allow us to obtain the horizontal creep flow of the ice shelf, and the vertical deviation due to tidal perturbations.

3.2.1 Perturbation factor

In order to obtain information on the velocity of Ronne Ice Shelf, we build interferograms from two images separated by 24 days for the Radarsat-1 images (1997) and 9 days for ERS-1 (1992). In Figure 1 we show the 92 interferogram together with the corresponding geocoded amplitude image. We also plot in Figure 3 several profiles across (profile AB) and along the rifts. Radar phase differences are converted into velocity. Using:

$$\phi_{ij} = \frac{4\pi}{\lambda}\left(-V_x \sin(\psi) + V_z \cos(\psi)\right)(t_j - t_i) + \frac{4\pi}{\lambda}(Z_i - Z_j)\cos(\psi) \tag{1}$$

where ϕ_{ij} is the flattened interferometric phase between images i and j, taken at epochs t_i and t_j, Z_i and Z_j are the corresponding vertical positions of the ice shelf (positive upwards), λ is the wavelength of the radar, ψ is the angle between the local vertical and the radar illumination direction, V_x and V_z are the horizontal and vertical velocity of the ice shelf, respectively, with the x axis parallel to the ground and perpendicular to the satellite track.

For an explanation of this formula, we refer the reader to Rignot (96). In Figure 1b, we calculated:

$$\begin{aligned} V &= \frac{\phi_{ij}}{\frac{4\pi}{\lambda}(t_j - t_i)\sin(\psi)} \\ &= -V_x + V_z \cot(\psi) + \frac{(Z_i - Z_j)}{t_j - t_i}\cot(\psi) \end{aligned} \tag{2}$$

which represents $-V_x$ modified by $[+V_z \cot(\psi) + (Z_i - Z_j)\cot(\psi)/(t_j - t_i)]$. Let us call P this vertical perturbation factor. We have to find a way to separate P from $-V_x$ in the interferograms. P contains a mixture of vertical motion due to creep, and motion due to tides. We will first evaluate

the contribution of the tidal term $(Z_i - Z_j)\cot(\psi)/(t_j - t_i)$, then we will study the horizontal ice shelf flow V_x, and finally we will see how to separate P from $-V_x$.

3.2.2 Tidal oscillations

As shown by Rignot (96), the tidal signal can be evaluated by applying a double difference technique with three or more radar images. This technique is applied here with a series of three different images acquired in February 92. If we call 1,2, and 3 the three images separated by 3 days, the double differencing of the phases gives:

$$\phi_{12} + \phi_{23} = \frac{4\pi}{\lambda}(2\,Z_2 - Z_3 - Z_1)\cos(\psi) \tag{3}$$

This double difference only depends on the tidal displacement and the incidence angle. Figure 4 shows the corresponding interferogram . Each fringe represents a change in elevation of 3.4 cm in 3 days. On a 10-km scale, the average tidal elevation differential ranges from 3 to 5 cm. This means for example that the ice constrained between rift 2 and 3 is 3 cm higher than the ice constrained between rift 3 and 4. Such a tidal oscillation could trigger a mode III fracture. We refer the reader to Andersen (95) for a presentation of the different fracture modes. Mode III fracture is due to the elevation differential between the two opposite flanks of the rift caused by tide.

It is hard to notice any perturbation of the tidal signal along or at the tip of any rift. This is important because P, the perturbation factor, will now be considered to be locally independent of the tidal process. On a large scale, however, the tidal component of the perturbation factor is on the order of 85 ma^{-1}, which represents about one tenth of V_x.

3.2.3 Horizontal displacement of the ice shelf

After this evaluation of the tidal influence on P, we can consider that locally (meaning on a scale of 10 km and less), we have $P \simeq V_z \cot\psi$. We have canceled the tidal contribution to P. In this paragraph, we will neglect P and observe the large-scale behaviour of the shelf around the rifts.

Figure 5 shows $-V_x$ for rift 3 in 92 and 97 respectively. Between 92 and 97, the looking directions differ by an angle of 9.9° so that the two images can be considered to first order to represent an evolution of V_x through time. It must also be considered that the direction of V_x is almost perpendicular to rift 3.

The most important feature to observe on a large scale, is the fringe rate on each side of the rift. On the left side, it is less than on the right one. This means that there is a difference in projected velocity between the two flanks of the rift. The corresponding velocity difference is responsible for the propagation of the rift. Figure 3b shows a plot for rift 3 of the velocity differential versus distance to the tip in 92 and 97. It can be seen on this plot that the velocity differential increases linearly from the tip, until it reaches a threshold where it becomes independent of the distance to the tip. This shows two different zones: one zone of pure rotation (20 km in 92, 30 km in 97) and a subsequent zone where the flanks of the rift are moving away from one another at a speed of 55 ma^{-1} in 92 and 62 ma^{-1} in 97. This observation implies that the active part to be taken into account in any fracture theory is smaller than the actual size of the rift.

4 Vertical displacement of the ice shelf

4.1 Observations

Let us recall the possible contributions to a vertical motion V_z of the ice shelf. A vertical displacement can be due to an accumulation rate, to a surfaace slope, to tidal oscillations or others effects.

For Ronne Ice Shelf, the accumulation rate is approximately 0.2 ma^{-1} (Giovinetto and others (2000)), which contributes $P = .46$ ma^{-1} if we take $\psi = 23.4°$.

The slope of the ice shelf contributes to the vertical component of the flowing velocity. As shown by Joughin and others (98), the vertical contribution is $P = V_x \cot(\psi) \tan(\alpha)$ where α is the slope in the satellite looking direction, if you assume the flow of the ice to be parallel to the ice shelf surface. Here, we have $\tan(\alpha) = 2\ 10^{-4}$, which contributes $P = .46$ ma^{-1}, which is on the same order as the vertical accumulation velocity. Finally, any vertical motion other than the tidal induced motions

can contribute to P.

We will now show how to separate $-V_x$ from P. ERS-1 was right looking in 1992 and Radarsat-1 was left looking during the AMM-1 Antarctic mission. As Table 1 shows, ERS-1 interferogram (3069-2940) is built in reference to the oldest amplitude image (orbit 2940), and Radarsat1 interferogram (9852-10195) is built in reference to the most recent image (orbit 10195). If we assume that Vz is the same in 92 and 97, we have in 92:

$$\phi_{92} = \frac{4\pi}{\lambda}(-V_x \sin(\psi) + V_x \cos(\psi)\tan(\alpha) + V_z \cos(\psi))\delta t_{92} \tag{4}$$

where we explicitely make the slope contribution appear, V_z is any vertical motion except that due to slope, and δt_{92} is 24 days. In 97, with Radarsat-1, we have:

$$\phi_{97} = \frac{4\pi}{\lambda}(-V_x \sin(\psi) - V_x \cos(\psi)\tan(\alpha) - V_z \cos(\psi))\,\delta t_{97} \tag{5}$$

where δt_{97} is 9 days.

Comparing equations (4) and (5), we note that the contribution $P = V_x \cot(\psi)\tan(\alpha) + V_z \cot(\psi)$ to the phase, changes signs between 92 and 97. In this transformation, we suppose to the first order that ψ is constant, which is almost the case ($\psi_{92} = 23.4°$ and $\psi_{97} = 28°$). We also consider the track directions to be the same (they differ by 9.9°). We finally assume that V_x and V_z are unchanged, at least to first order.

In Figure 5, apart from the large scale horizontal behaviour, we observe patterns along the flanks of the rift and at the tip of the rift. These patterns are better detected if we take the derivative of the signal. This is shown in Figure 6 ,which gives a view of all the rifts. In this figure, the background horizontal creep is homogeneous and the patterns around the rifts are more visible .

If we come back to Figure 5, we can notice how in 92 and 97, the patterns are opposed. This is particularly true at the tip, where in 92, the fringes can be seen to point towards the tip, whereas in 97, the fringes point outwards. As we have seen in equations (4) and (5), this type of reversal is characteristic of a vertical motion. Since the tidal perturbation near the rifts is inexistent, and since

any slope induced vertical displacement would yield a dissymetry in slope, we conclude that these patterns are due to a vertical creep, not to tide.

Figure 7a and 7c (left parts) show the vertical motion for rift 3 and 5 in 97. We have eliminated $-V_x$ by fitting on each side of the rift a linear fit to $-V_x$. This allows us to eliminate even the velocity differential spotted in Figure 3. It can be seen that in each case, two bands of positive V_z are present, as can be seen in the Figure 7b and 7d. Bands are 1 km wide and V_z reaches values of .8 ma^{-1}. In the immediate vicinity of the rifts, V_z becomes strongly negative. It is also the case at the tip of the rift: there is a concentration of negative velocity, which gives this characteristic pattern to the fringes in Figure 5.

We find the tip patterns to be similar in rifts 1,2 and 3, the most active ones. In the case of rifts 4 and 5, which are inactive, the bands of positive V_z are still present, but the tip pattern is absent. We also find bands of positive velocity at the ice front. This leads us to model this deformation as resulting from a hydrodynamic creep of the ice shelf.

4.2 Hydrodynamic creep of the ice shelf

We have seen that along the rifts and at the tip, vertical perturbations are visible. To explain those perturbations, we use a model developped by Reeh (68) to explain the calving of iceberg, which we generalize to apply to a 2-D plate. Basically, the idea is that the hydrodynamic pressure of the water on the faces of the rift bends the ice shelf along the sides of the rift, generating a vertical motion which is detected in our interferograms. For a complete explanation of the concepts, we refer the reader to Reeh (68). We present the model and the finite element implementation in detail in Appendix 1.

To validate our model, we replicated the simulation results of Reeh in one dimension and verified that we indeed obtained the same results. Figure 8a shows the evolution of a profile perpendicular to the rift. It can be seen, that perpendicular to the rift, V_z reaches a maximum about 500 m from the rift. This maximum decreases in intensity with time, and the profile translates towards the rift. This

maximum is the one responsible for the narrow bands observed along the rifts. Figure 8b shows the evolution of the maximum values with time for different viscosities,μ (Figure 8b). It can be seen that V_{zmax} decreases asymptotically with time, and that the rate of decrease is inversely proportional to μ.

The generalization of the model to a plate, allows for the interpretation of the tip patterns as well. We have conducted a static (no propagation) and dynamic modelling of the rupture. In the dynamic case, we artificially opened the mesh at the tip of the rift at each time increment. The geometric configuration of the plate we use is shown in Figure 9a.

4.2.1 Static case

To match the model with the observations, we conduct calculations with different widths e. We obtain a good fit with $e > 3000$ m.

In order to chose our model viscosity, we compute a viscosity profile from the velocity maps we have, using:

$$\sigma' = B\,\dot{\varepsilon}^{\frac{1}{3}} \tag{6}$$

where σ' is the stress deviator, $\dot{\varepsilon}$ the strain rate and B the flow constant which depends on the temperature and ice constitution. We can deduce μ (Rignot and Mac Ayeal (98)):

$$\mu = \frac{B}{2(\frac{\partial V_x}{\partial x}^2 + \frac{\partial V_y}{\partial y}^2 + \frac{1}{4}(\frac{\partial V_x}{\partial y} + \frac{\partial V_y}{\partial x}^2 + \frac{\partial V_x}{\partial x}\frac{\partial V_y}{\partial y})^{\frac{1}{3}})} \tag{7}$$

For B, we use $B = 2.1\ 10^8$ Pa $s^{-\frac{1}{3}}$. The viscosities obtained from the observations are in the range 10^{13} to 10^{15} Pa s, with the largest values recorded far from the rifts and the smaller ones near the rifts. If we input the observed viscosity profile in our model, we find that the results remain the same if we chose a constant model viscosity $\mu = 10^{14}$ Pa s.

Another way of chosing the model viscosity is by computing the evolution of V_{zmax} in time, for different viscosities (Figure 8b). We superimpose these curves with the observed values of V_{zmax} for

the different rifts. The age of each rift is estimated from the distance to Hemmen Ice Rise and the mean ice shelf velocity. The best fit is obtained for $\mu = 10^{14}$ Pa s. Note that rift 4 deforms more rapidly. We will explain this in the discussion.

In either case, $\mu = 10^{14}$ Pa s proves to be the best value for the model viscosity. We show the results of the computation together with the vertical velocity map in 1997 for rift 5, in Figure 7a. Figure 7b also shows a comparison between the observations and the model on three profiles taken perpendicular to the rift. We use the following input data: $\mu = 10^{14}$ Pa s, $L = 30$ km, $2e = 12$ km, $\rho_{water} = 1023$ kg m^{-3}, $\rho_{ice} = 917$ kg m^{-3}and $h = 500$ m where L is the length of the plate, $2e$ the width, ρ_{water} the water density, ρ_{ice} the ice density and h the ice thickness. We carry the computation over a period of 40 years.

Figure 7a and 7b show a good fit between observations and model. The tip deformation pattern is absent in the two cases, which confirms that rift 5 is not propagating. We had seen it was the case in Table 2 from the observed propagation rates. Near the edges of the rift, our model predicts that V_z becomes strongly negative. In the observations,however this cannot be assessed because we do not have a reliable signal in this area. Nevertheless, the observed V_z decreases near the edges, which is consistent with the model.

4.2.2 Dynamic case

In the dynamic model, the crack is artificially opened. At each time increment, we open one cell of the mesh in front of the rift. The value of μ and the size of the cell determine the propagation rate of the rift. The results are shown in Figure 7c and 7d, together with the observations for rift 3 in 97. As for rift 5, we show the velocity map and the profiles. The propagation rate in the model is 300 ma^{-1}.

Rift 3 exhibits the same V_z positive bands along the rift, but the deformation at the tip is different. If we compare the observations in Figure 7a and 7c, we see that a wide pattern develops. The positive bands (yellow) circle around the tip and a strong negative singularity (blue) develops at the tip. The

model accounts well for these modifications, which suggests that the tip pattern modification is characteristic of an actively propagating rift.

Some discrepancies between the model and the observations appear in profile 3 of Figure 7d. The magnitude of V_z is too large in the model, near the tip of the rift. We have checked that this discrepancy is not due to the choice of μ. We attribute it to the simplification of our generalized viscous plate model. To evaluate the propagation rates of rifts from the magnitude of tip deformation patterns is therefore a difficult problem, and we have not made any attempt to pursue this aspect of the study.

We have taken care to open the mesh at each time increment, which means that the rupture process in our model is continuous. The good fit between the model and the observations is a strong indicator that this hypothese is correct. This is of great importance for the application of Linear Elastic Fracture Mechanics discussed next.

5 Elastic fracture singularity

We have seen in the previous paragraph that the tip pattern can be interpreted as a vertical hydrodynamic creep of the ice shelf. We now verify that this pattern is not influenced by the concentration of stress predicted by the Linear Elastic Fracture Mechanics, which could lead to a horizontal velocity pattern as the rift opens. As can be seen on Figure 6, the ice shelf has an almost uniform positive strain rate, which leads to an opening of the rifts with a mode I fracture (Anderson p53).

LEFM predicts the displacement jump across a rift in mode I to be (Hellan p237):

$$\Delta u = \frac{K_I}{G}\sqrt{\frac{r}{2\pi}}\frac{4}{1+\nu}$$

where r and θ are polar coordinates, Δu the displacement jump (figure 9b), K_I is the stress intensity factor and G is the shear modulus of ice.

The rift is propagating at a rate $v = \frac{\partial r}{\partial t}$, we have:

$$\Delta v = 2\frac{K_I}{E}\frac{v}{\sqrt{2\pi r}}$$

where E is the young modulus.If we use $K_I = .2$ MPa $m^{-1/2}$ (Mulmule and Dempsey (2000)), $v = 1000$ ma^{-1} and E=9 10^9 Pa (Petrenko p39), we get:

$$\Delta v = \frac{5.6\ 10^{-10}}{\sqrt{r}}$$

In order to observe such a signal with INSAR, Δv should be at least .1 m a^{-1}, which gives $r \leq 4$ cm. This is much less than the resolution cell (7m) of the radar, so the singularity is not observable in our interferograms.

Nevertheless, as shown by Mulmule and Dempsey (2000), the behaviour of large cracks in tabular ice plates of size ≥ 200 m should be well explained by LEFM. On a large scale, we can assume that the ice shelf behaves like a cracked rigid body in translation, and predict the propagation rate of rifts. Propagation is assumed to be continuous and the shelf to behave like a double cantilevered beam of thickness h submitted to a constant stress on the flanks of the rift. Figure 9b shows the geometry used for this modelling.

The displacement jump Δu is (efunda 2002):

$$\Delta u(x) = h\,\sigma\,\frac{x^2\,(6\,a^2 - 4\,ax + x^2)}{12\,E\,I} \tag{8}$$

where Δu is the distance between the two flanks of a rift, at distance x from the tip. I is the moment of inertia of the beam ($I = h\,e^3/12$), e is the distance between two rifts. Following the LEFM, the action of external forces on a rift can be reduced to the action of a stress σ on the flanks of the rift (Andersen p66.). We will work under the assumption that σ is constant.

We calculate the strain energy due do this repartition of stress on the flank of the rift:

$$U = \frac{\sigma^2 h^2}{2EI}\frac{a^5}{5} \tag{9}$$

The driving force ϕ is derived from (Andersen p43.):

$$\phi = \frac{1}{h}\left(\frac{\partial U}{\partial a}\right)_{\sigma} \tag{10}$$

which yields:

$$\phi = \frac{\sigma^2 h}{EI} a^4 \tag{11}$$

In order to eliminate σ which is unknown, we use equation (8) at $x = a$, and we obtain:

$$\phi = \frac{\alpha \Delta u(a)^2}{a^4} \tag{12}$$

where $\alpha = 4EI/h$.

At the rupture point, we have $\phi = R$ where R is the resistance of the ice shelf. Therefore, if we derivate the equation $\phi = R$ in time, we obtain:

$$v = \frac{da}{dt} \tag{13}$$

$$= \frac{\Delta \dot{u}(a)}{\Delta u(a)} \frac{1}{(\frac{2}{a} + \frac{1}{2R}\frac{dR}{da})} \tag{14}$$

We make another hypothesis which is that the resistance $R(a)$ is constant and independent of a, ie brittle fracture. In this case, we have

$$v = \frac{\Delta \dot{u}(a)}{\Delta u(a)} \frac{a}{2} \tag{15}$$

If we make the hypothesis that the rupture is at the limit of instability, we have:

$$\phi = R \tag{16}$$

$$\frac{d\phi}{da} = \frac{dR}{da} \tag{17}$$

We then have the following result:

$$v = \frac{\dot{\Delta u}(a)}{\Delta u(a)} \frac{a}{4} \tag{18}$$

The two formulas (15) and (18) can be easily confronted to the velocity maps we have. We can evaluate the quantity $(\frac{\dot{\Delta u}}{\Delta u}\frac{a}{2})$ at the end of the rift near HIR, as determined in Figure 3b, and predict a propagation rate for the rift.

Figure 10 shows the results. We plotted the observed positions of rifts 1,2 and 3 between 1992 and 1998 and the modeled positions with propagation rates evaluated from the velocity maps in 1992 and 1997 using equation (15). The propagation is overestimated with the rate evaluated in 92, which suggests the ice shelf was unstable at that time. The fit is good with the propagation rate evaluated in 97, which suggests a stable propagation.

6 Discussion and Conclusions

The conclusions of this article are based on observations of vertical creep velocities that are three orders of magnitude smaller than the horizontal creep velocities. In order to observe the corresponding patterns, we had to choose long time spans between multiple INSAR passes (ERS-1 9 days, Radarsat 24 days). Therefore, the quality of the interferograms had to be excellent in order for the observations to be possible.

In the case of Ronne Ice Shelf, we managed to observe with a good precision the tidal oscillations, and concluded that an elastic fracture in mode III is unlikely. Yet the fatigue associated with long term tidal oscillations (22000 cycles in 30 years) could play an important role in the propagation of rifts, which we have not yet been able to explore.

The observed vertical creep is explained by a viscous plate model. This model has simplifying assumptions which must be discussed here. The main assumption is that the ice shelf behaves like a plate. At the tip of the rift and near the edges, this hypothesis not evident. Neither the temperature

variations nor the non linear caracter of the viscosity are taken into account, a nd the influence of the calving process has not been considered: we work under the hypothesis that the edges of the rifts do not calve. But as Reeh showed in his study, the surface strain produced by a bending of the ice shelf is at the origin of the calving of icebergs. The anomaly spotted in Figure 8b for rift 4 could be due to calving events that increased the vertical velocity. This could also be the main reason for the presence of debris ice in the rifts discussed by Rignot and Mac Ayeal (1998). Taking into account this calving process could lead to an increase in the predicted vertical velocity, or a decrease in the viscosity used to model the observations.

The precise evaluation of propagation rates of the rifts from the tip deformation patterns is a difficult problem. The differences between model and observations in Figure 7d (profile 3) show that linking V_{zmax} at the tip of the rift to the propagation rate is difficult. One last observation previously made by Reeh (68) is the absence of undulations predicted by the model in the data. Figure 8a shows that at a distance of 4 thicknesses, the model predicts a second peak of vertical velocity. This is not observed in the velocity maps, even on the older rifts. This inconsistency has yet to be resolved.

Despite these limitations, the tip pattern is well explained by the viscous model, which suggests that the propagation of rifts is a continuous process. The instability of the rifts will result from an evolution of the resistance $R(a)$, as discussed in last section. This instability can be forecasted from the dynamic and geometrical properties of the ice shelf. A key factor is the driving stress applied to the rift. By modelling the rift as a cracked double cantilevered beam, we made a strong assumption on the nature of the driving force but this assumption yields results of the same order of magnitude as the observed propagation rates.

The difference between predicted and observed velocities can be explained by the non brittle character of the rupture or by the instability of the propagation. In order to get more precise results, the resistance $R(a)$ and the origin of the driving force ϕ must be evaluated, which necessitates more interferograms at different times.

7 Acknowledgements

This work was performed at the Jet Propulsion Laboratory, California Institute of Technology, under a contract with the National Aeronautics and Space Administration, Cryospheric Sciences Program. We thank the European Space Agency, the VECTRA project and Alaska SAR Facility for distributing the radar data employed in this study. We also thank Marjorie Schmetlz for her help in the images processing and the finite element modelling.

8 Appendix: vertical hydrodynamic creep model

8.1 Modelling

We will only show here the modifications used to generalise the Reeh 1D viscous beam model to a 2D viscous plate model. The geometry used for the modelisation is shown in Figure 9a The dimensions of the plate model are chosen in order to correspond to the rift 3 configuration.

We begin with the well known equations of a floating plate:

$$\frac{\partial M_x}{\partial x} + \frac{\partial M_{xy}}{\partial y} - Q_x = 0 \tag{19}$$

$$\frac{\partial M_{xy}}{\partial x} + \frac{\partial M_y}{\partial y} - Q_y = 0 \tag{20}$$

$$\frac{\partial Q_x}{\partial x} + \frac{\partial Q_y}{\partial y} + \rho_w g Z = 0 \tag{21}$$

where M_x, M_y, M_{xy} are the hydrodynamic moments over a section of the ice shelf, Z is the elevation of the ice shelf, Q_x, Q_y are the vertical shear forces, ρ_w is the density of the water and g the gravity acceleration. Derivating equations (19) and (20) and using (21) gives:

$$\frac{\partial^2 M_x}{\partial x^2} + 2\frac{\partial^2 M_{xy}}{\partial x \partial y} + \frac{\partial^2 M_y}{\partial y^2} + \rho_w g Z = 0 \tag{22}$$

We choose a viscous model, because the characteristic times of the phenomena observed are on the order of one year. In this case, we have the following links between elevation Z and the hydrodynamic moments:

$$\frac{\partial}{\partial t}\frac{\partial^2 Z}{\partial x^2} = \frac{3}{\mu h^3}\left(M_x + \frac{\rho_i g h^3}{12}\right) \tag{23}$$

$$\frac{\partial}{\partial t}\frac{\partial^2 Z}{\partial x \partial y} = \frac{3}{\mu h^3}(M_{xy}) \tag{24}$$

$$\frac{\partial}{\partial t}\frac{\partial^2 Z}{\partial y^2} = \frac{3}{\mu h^3}(M_y + \frac{\rho_i g h^3}{12}) \tag{25}$$

where μ and ρ_i are the viscosity and the density of ice and h is the thickness of the ice shelf. Replacing (23),(24),(25) in (22) we obtain the ruling equation for the viscous vertical creep of an ice shelf:

$$\frac{\partial}{\partial t}\nabla^4 Z + DZ = 0 \text{ where } D = \frac{3\rho_w g}{\mu h^3} \tag{26}$$

In order to solve the problem using a Finite Element Formulation, we have to find the boundary conditions. We model rift 3 as a single independent rift. The rift is propagating across a tabular segment. On the edges of this segment, we have:

$$Z = 0 \tag{27}$$

$$\vec{\nabla} Z = 0 \tag{28}$$

We will discuss these assumptions further ahead. The crack is modelled as the reunion of two faces separated by a zero distance. This corresponds to the observations: the rifts are very sharp near their tips. On these faces, the repartition of the water pressure gives a moment that will bend the shelf.

If $\vec{m}$ and $\vec{n}$ are the normal and tangent vectors to the rift faces, we have:

$$\sigma \vec{m} \vec{m} = P_w \tag{29}$$

$$\sigma \vec{m} \vec{n} = 0 \tag{30}$$

$$\sigma \vec{m} \vec{z} = 0 \tag{31}$$

with P_w the water pressure, and σ the stress tensor.

Equation (31) gives, if we consider $\vec{m} = [m1, m2]$ and $\vec{n} = [n1, n2]$,

$$\sigma_{xz} m_1 + \sigma_{yz} m_2 = 0$$

The integration of this equation along the vertical axis, leads to:

$$Q_x m_1 + Q_y m_2 = 0$$

And if we use equations (19) and (20),

$$(\frac{\partial M_x}{\partial x} + \frac{\partial M_{xy}}{\partial y})m_1 + (\frac{\partial M_{xy}}{\partial x} + \frac{\partial M_y}{\partial y})m_2 = 0$$

which in turn gives, if we use equations (23),(24) and (25),

$$\vec{\nabla}(\nabla^2 Z).\vec{m} = 0 \tag{32}$$

Equation (29) develops into

$$(\sigma_y - \sigma_x)m_1 m_2 + (m_1^2 - m_2^2)\sigma_{xy} = 0$$

which gives after integration:

$$(M_y - M_x)m_1 m_2 + (m_1^2 - m_2^2)M_{xy} = 0 \tag{33}$$

Equation (30) develops into

$$\sigma\vec{m}.\vec{m} = \sigma_x m_1^2 + 2\sigma_{xy} m_1 m_2 + \sigma_y m_2^2 = P_w$$

after integration, we have:

$$M_x m_1^2 + 2M_{xy} m_1 m_2 + M_y m_2^2 = M_{mm}$$

where M_{mm} is the hydrodynamic moment due to the w pressure. This moment has been calculated by Reeh.

$$M_{mm} = \frac{\rho_w g h^3}{12}(-3d_i^2 + 2d_i^3 + 6(d_i - d_i^2)\frac{Z}{h})$$

where $d_i = \rho_i/\rho_w$ We therefore have:

$$M_x m_1^2 + 2M_{xy} m_1 m_2 + M_y m_2^2 = M_{mm} = \frac{\rho_w g h^3}{12}(-3d_i^2 + 2d_i^3 + 6(d_i - d_i^2)\frac{Z}{h}) \tag{34}$$

In order to have a closed formulation, equation (33) together with equation (34) are not enough. We need the third equation:

$$\frac{\partial}{\partial t}\frac{\partial^2 Z}{\partial m^2} = 0 \tag{35}$$

where $\frac{\partial}{\partial m} = \vec{\nabla} Z.\vec{m}$. This is true along the rift. In order to simplify, let us suppose the rift to be along the x axis,we then have with equations (33),(34) and (35) and equations (23),(24) and (25):

$$\frac{\partial}{\partial t}\frac{\partial^2 Z}{\partial x^2} = 0 \tag{36}$$

$$\frac{\partial}{\partial t}\frac{\partial^2 Z}{\partial y^2} = \frac{\rho_w g h^3}{12}(di - 3d_i^2 + 2d_i^3 + 6(d_i - d_i^2)\frac{Z}{h}) \tag{37}$$

at the rifts.

8.2 Finite element formulation

We use different formulations to build the finite element solution. The most appropriate is a mixed-formulation with nodal functions of first degree and triangular elements.

The time iteration is an euler implicit scheme always stable. In order to run calculations for the dynamic cases of propagation of the rifts, we open the mesh at each time increment and use different meshes or different time steps to compute solutions with different propagation rates. The results of the dynamic cases prove to be stationary after 20 to 30 time iterations.

In order to check the validity of our formulation, the numerical procedure used by Reeh to solve his problem in 1 dimension has been implemented and yields to the same results.

The scheme is stable upon refinement of the mesh and we have checked the singularity with a 30000 elements mesh in the stable case. The singularity is well accounted for even with a lesser number of elements, we therefore use 3000 elements for the dynamic case.

In the dynamic case, the mesh is artificially opened in the direction of propagation at the tip of the rift. We verified that the mesh was symmetric with respect to the x axis

REFERENCES

Anderson T.L. 1995. Fracture mechanics. Fundamentals and applications. Second Edition.

Bazant Z.P. 2002. Scaling of Sea Ice Fracture. *J. of App. Mech.*,**69**, 11-24 January.

Doake C.S.M., Corr H.F.J., Rott H., Skvarca P. Young N.W. 1998. Breakup and conditions for stability of the northern Larsen Ice Shelf, Antarctica.*Nature.*,**391** 778.

Efunda Engineering Fundamentals.
http://www.efunda.com/formulae/solid_mechanics/beams/casestudy_bc_cantilever.cfm

Giovinetto M.B. Zwally H.J. 2000. Spatial distribution of net surface accumulation on the antarctic ice sheet.*Ann. of Glaciol.*,**31** 171.

Hellan K. 1984. Introduction to fracture mechanics. Mc Graw-Hill Book Company.

Jacobs, S.S., H.H. Helmer, C.S.M. Doake, A. Jenkins and R.M. Frolich. 1992. Melting of ice shelves and the mass balance of Antarctica. *J. Glaciol.*,**38** (130), 375-387.

Joughin, I.R., Kwok, R and Fahnestock, M.A. 1998. Interferometric estimation of three-dimensional ice-flow using asending and descending passes. *IEEE Transactions on geoscience and remote sensing* .,**36** (1), January.

Mulmule S.V. and Dempsey J.P. 2000. LEFM size requirements for the fracture testing of sea ice *Int. J. Frac.* **102** 85-98.

Petrenko F.V. and Whitworth R.W. Physics of ice. 1998. Oxfort University Press.

Reeh N. 1968. On the calving of ice from floating glaciers and ice shelves. *J. Glaciol.*,**7** (50).

Rignot, E. 1996. Tidal motion, ice velocity and melt rate of Petermann Gletscher, Greenland, measured from radar interferometry. *J. Glaciol.*,**42** (142).

Rignot, E and MacAyeal, D.R. 1998. Ice-Shelf dynamics near the front of the Filchner-Ronne ice Shelf, Antarctica, revealed by SAR interferometry. *J. Glaciol.*, **44** (147) 405-417.

Sanderson, T.J.O. 1979. Equilibrium profile of ice shelves. *J. Glaciol.*, **22** (88), 435-460.

Table 1. Radar images used to study the period preceding calving of iceberg A38.

Amplitude images used to acces propagation rates of rifts		
Date	Orbit	Satellite
1992 2/16/92	3069	ERS1
1996 2/23/96	24098	ERS1
1997 10/17/97	10195	Radarsat1
1998 2/2/98	14574	ERS-2

Interferograms used to acces fields of horizontal and vertical velocities			
Date	Orbit	Satellite	Interferograms
1992 2/7/92	2940	ERS1	3069-2940
1992 2/16/92	3069	ERS1	Simple difference
1997 9/23/97	9852	Radarsat1	9852-10195
1997 10/17/97	10195	Radarsat1	Simple difference
1992 2/10/92	2983	Radarsat1	3026-2983-5499
1992 2/13/92	3026	Radarsat1	Double difference
1992 2/16/92	5499	Radarsat1	

Table 2. Propagation rates of rifts between 92 and 98

Period	Rate in ma^{-1}					Imprecision
	1	2	3	4	5	
2/16/92 $->$ 2/23/96	75	920	1010	0	-170	50
2/23/96 $->$ 10/17/97	3140	370	524	-90	-90	120
10/17/97 $->$ 2/2/98	1390	3480	4520	N/A	N/A	700

Processes involved in the propagation of rifts near Hemmen Ice Rise in the Ronne Ice Shelf, Antarctica.

Eric Larour*, Eric Rignot*, and Denis Aubry**
* *Jet Propulsion Laboratory, California Institute of Technology, Pasadena 91109, California, U.S.A.*
** *Laboratoire de Mecanique des Sols, Structures et Materiaux, Ecole Centrale Paris, Paris, France*

ABSTRACT

We use radar interferometric images collected by ERS-1 and Radarsat-1 to observe the rupture tip of rifts along Hemmen Ice Rise on the Ronne Ice Shelf, Antarctica. Interferograms generated in 1992 and 1997 allow us to observe the deformation of ice accumulated over respectively 9 and 24 days. We combine these interferograms together to separate the continuous process of creep deformation from the more cyclic motion caused by variations in ocean tides. Then, we confront the observations with a deformation model for ice and obtain the following results: 1) The tidal oscillation of the Ronne Ice Shelf only yields small deformations near the tip of rifts. 2) Along the rifts, the icefront and at the rupture tips, vertical creep is observed and well explained by a model of viscous deformation of ice. Furthermore, the deformation pattern observed around the rupture tips can be used to determine whether the rift propagation is active or blocked. 3) The deformation pattern predicted by linear elastic fracture mechanics is too weak compared to the viscous adjustment of the ice, to be observed, but the propagation rate of the rifts is well explained by linear elastic fracture mechanics. These results are an important step towards developing a better model of ice-shelf calving mechanism.

1 Introduction

Iceberg calving plays a key role in the evolution of ice shelves. It controls a large fraction of the ice discharge into ocean (Jacobs and others (1992)) and involves important processes, for example the formation and propagation of rifts, which influence the mechanical stability of ice shelves (Doake and others 1998).

A good understanding of the mechanisms involved in the calving process is therefore necessary. Some of the main unknown characteristics of iceberg calving are the timing of calving events, the origin of the breakup of tabular icebergs, the origin of the rifts that give birth to giant icebergs, the mode and rate of propagation of the rifts, and what controls them.

All these factors are important to establish a calving law which will allow a model of calving mechanisms on an ice shelf. In this article, we focus our attention on the eastern sector of the Ronne Ice Shelf. On October 13^{th} of 1998, in the zone surrounding Hemmen Ice Rise near Berkner Island, a tabular iceberg of 145x50 km^2 in size broke off from the ice shelf. This was one of the largest calving events ever witnessed in Antarctica. The fact that it originated from a prexisting rift which was part of a larger field of rifts around Hemmen Ice Rise, with satelite imagery (INSAR) collected before and after, makes it an ideal event to study calving mechanisms.

In this article, we use radar images covering a period of 6 years before the final breakup. These radar images are processed interferometrically in order to obtain both the horizontal and vertical velocity of the ice shelf. We also use the amplitude imagery to measure the propagation rate of the rifts emmanating from Hemmen Ice Rise and the evolution of the geometry of those rifts. We analyse this information to understand the ice shelf evolution prior to calving.

The discussion presents a series of results. First, we show that the process associated with the tidal motion of the Ronne Ice Shelf influence very little the propagation of rifts and that the main contribution to their propagation comes from the horizontal flow of the ice shelf. Then we present an explanation of the origin of the deformation pattern observed near the rift tips with INSAR using

a viscous model of ice. We use these patterns to characterize the fracturing process. We show that the stress distribution around the tip of the rifts is too weak to be observed with an interferogram, and masked by the viscous adjustment of the ice-shelf to the propagation of the rupture. We measure propagation rates of the Ronne Ice Shelf rifts with predictions for linear elastic fracture mechanics. We conclude by discussing how these results will help develop a better modelization of fracture processes on an ice-shelf.

2 Study area

Hemmen Ice Rise, Ronne Ice Shelf, lays on the eastern flank of Berkner Island (Figure 1a). This ice rise is at the origin of a vast field of rifts, some having a length of up to 40 km. Crevasses originating from the shear margin of the ice rise, transform into rifts and propagate parallel to the ice front at rates about 1000 ma^{-1}, which is comparable to the ice shelf velocity. On October 13^{th} 1998, the rift marked number 3 on Figure 1a became unstable and broke off, giving birth to tabular iceberg A 38 of 145 km in length.

The complex pattern of ice motion around HIR prior to calving was discussed in details by Rignot and Mc Ayeal (1998). The ice shelf flows with a decreasing velocity along the flanks of Berkner Island, and there is a general rotation of the ice shelf around Berkner Island towards the east. Yet the presence of the rise as an anchor to the ice shelf, and the formation of ice melange between the rifts,are at the origin of a counter rotation: in Figure 1a, rifts 1 and 2 which are still attached to Hemmen Ice Rise rotate eastwards, but rifts 3,4 and 5, which are free from the rise, rotate towards the west. This rotation is at the origin of the opening of crevasses which form rifts and propagate parallel to the ice front.

3 Observations

We use interferograms built from ERS-1 and 2 and Radarsat-1 radar satellites at two different epochs, 1992 and 1997, prior to the event of 1998. These interferograms allow us to observe the de-

formation of ice accumulated over respectively 9 and 24 days. We combine these interferograms in different ways to separate the continuous process of creep deformation from the more cyclic motion due to ocean tides. We also use the radar images to evaluate changes in geometry, and propagation rate of the rift. Table 1 summarises the images we used and the combinations we made.

3.1 Geometrical observations

From the amplitude images in 1992, 1996, 1997 and 1998, we measure the propagation rates of the opening rifts. The radar amplitude images are geocoded at a sample spacing of 50 m on a polar stereographic grid. We measure the difference in length of the rifts, between the four radar images, by detecting characteristic features along the rifts which are common between images. We give the results in Table 2.

It can be seen that rifts 4 and 5 are basically inactive. In fact, the rates given in Table 2 are more or less at the noise level. This observation is confirmed by the fact that the imprints of rifts 4 and 5 were still visible on iceberg A38 (Figure 2b). This inactivity may be due to the sea ice filling the rifts or to the deconnection from HIR. The nearer the icefront, the thicker is this layer of ice, which gives cohesion to the flanks of the rift, as demonstrated by Rignot and Mac Ayeal (98). Also, the lateral shear is less important far from HIR, which makes it harder for the rifts to propagate.

Rifts 1,2 and 3 are the most active. Rifts 2 and 3 show a similar pattern of propagation. If we make the assumption that the propagation is continuous, we find that rifts 2 and 3 decelerated between 92 and 97, and accelerated suddenly in 3 months at the beginning of 98. The final rupture of rift 3 took place on October 1998, 7 months later. Rift 1 did not propagate during 4 years between 92 and 96, but started to propagate again at high velocity in 1997. This is consistent with the position of rift 1 along the ice rise margins: it is located (Figure 1a and 2a) at a point where the bay sides diverge. Sanderson (79) has shown that at this point, the strain rate reaches a maximum, therefore facilitating a sudden propagation of rifts, and ice-shelf calving.

3.2 Dynamics of the ice shelf

We use interferograms to characterize the ice shelf dynamics. Different combinations of interferograms allow us to obtain the horizontal creep flow of the ice shelf, and the vertical deviation due to tidal perturbations.

3.2.1 Perturbation factor

In order to obtain information on the velocity of Ronne Ice Shelf, we build interferograms from two images separated by 24 days for the Radarsat-1 images (1997) and 9 days for ERS-1 (1992). In Figure 1 we show the 92 interferogram together with the corresponding geocoded amplitude image. We also plot in Figure 3 several profiles across (profile AB) and along the rifts. Radar phase differences are converted into velocity. Using:

$$\phi_{ij} = \frac{4\pi}{\lambda}\left(-V_x \sin(\psi) + V_z \cos(\psi)\right)(t_j - t_i) + \frac{4\pi}{\lambda}(Z_i - Z_j)\cos(\psi) \tag{1}$$

where ϕ_{ij} is the flattened interferometric phase between images i and j, taken at epochs t_i and t_j, Z_i and Z_j are the corresponding vertical positions of the ice shelf (positive upwards), λ is the wavelength of the radar, ψ is the angle between the local vertical and the radar illumination direction, V_x and V_z are the horizontal and vertical velocity of the ice shelf, respectively, with the x axis parallel to the ground and perpendicular to the satellite track.

For an explanation of this formula, we refer the reader to Rignot (96). In Figure 1b, we calculated:

$$\begin{aligned} V &= \frac{\phi_{ij}}{\frac{4\pi}{\lambda}(t_j - t_i)\sin(\psi)} \\ &= -V_x + V_z \cot(\psi) + \frac{(Z_i - Z_j)}{t_j - t_i}\cot(\psi) \end{aligned} \tag{2}$$

which represents $-V_x$ modified by $[+V_z \cot(\psi) + (Z_i - Z_j)\cot(\psi)/(t_j - t_i)]$. Let us call P this vertical perturbation factor. We have to find a way to separate P from $-V_x$ in the interferograms. P contains a mixture of vertical motion due to creep, and motion due to tides. We will first evaluate

the contribution of the tidal term $(Z_i - Z_j)\cot(\psi)/(t_j - t_i)$, then we will study the horizontal ice shelf flow V_x, and finally we will see how to separate P from $-V_x$.

3.2.2 Tidal oscillations

As shown by Rignot (96), the tidal signal can be evaluated by applying a double difference technique with three or more radar images. This technique is applied here with a series of three different images acquired in February 92. If we call 1,2, and 3 the three images separated by 3 days, the double differencing of the phases gives:

$$\phi_{12} + \phi_{23} = \frac{4\pi}{\lambda}(2\,Z_2 - Z_3 - Z_1)\cos(\psi) \tag{3}$$

This double difference only depends on the tidal displacement and the incidence angle. Figure 4 shows the corresponding interferogram . Each fringe represents a change in elevation of 3.4 cm in 3 days. On a 10-km scale, the average tidal elevation differential ranges from 3 to 5 cm. This means for example that the ice constrained between rift 2 and 3 is 3 cm higher than the ice constrained between rift 3 and 4. Such a tidal oscillation could trigger a mode III fracture. We refer the reader to Andersen (95) for a presentation of the different fracture modes. Mode III fracture is due to the elevation differential between the two opposite flanks of the rift caused by tide.

It is hard to notice any perturbation of the tidal signal along or at the tip of any rift. This is important because P, the perturbation factor, will now be considered to be locally independent of the tidal process. On a large scale, however, the tidal component of the perturbation factor is on the order of 85 ma^{-1}, which represents about one tenth of V_x.

3.2.3 Horizontal displacement of the ice shelf

After this evaluation of the tidal influence on P, we can consider that locally (meaning on a scale of 10 km and less), we have $P \simeq V_z \cot\psi$. We have canceled the tidal contribution to P. In this paragraph, we will neglect P and observe the large-scale behaviour of the shelf around the rifts.

Figure 5 shows $-V_x$ for rift 3 in 92 and 97 respectively. Between 92 and 97, the looking directions differ by an angle of 9.9° so that the two images can be considered to first order to represent an evolution of V_x through time. It must also be considered that the direction of V_x is almost perpendicular to rift 3.

The most important feature to observe on a large scale, is the fringe rate on each side of the rift. On the left side, it is less than on the right one. This means that there is a difference in projected velocity between the two flanks of the rift. The corresponding velocity difference is responsible for the propagation of the rift. Figure 3b shows a plot for rift 3 of the velocity differential versus distance to the tip in 92 and 97. It can be seen on this plot that the velocity differential increases linearly from the tip, until it reaches a threshold where it becomes independent of the distance to the tip. This shows two different zones: one zone of pure rotation (20 km in 92, 30 km in 97) and a subsequent zone where the flanks of the rift are moving away from one another at a speed of 55 ma^{-1} in 92 and 62 ma^{-1} in 97. This observation implies that the active part to be taken into account in any fracture theory is smaller than the actual size of the rift.

4 Vertical displacement of the ice shelf

4.1 Observations

Let us recall the possible contributions to a vertical motion V_z of the ice shelf. A vertical displacement can be due to an accumulation rate, to a surfaace slope, to tidal oscillations or others effects.

For Ronne Ice Shelf, the accumulation rate is approximately 0.2 ma^{-1} (Giovinetto and others (2000)), which contributes $P = .46\ ma^{-1}$ if we take $\psi = 23.4°$.

The slope of the ice shelf contributes to the vertical component of the flowing velocity. As shown by Joughin and others (98), the vertical contribution is $P = V_x \cot(\psi) \tan(\alpha)$ where α is the slope in the satellite looking direction, if you assume the flow of the ice to be parallel to the ice shelf surface. Here, we have $\tan(\alpha) = 2\ 10^{-4}$, which contributes $P = .46\ ma^{-1}$, which is on the same order as the vertical accumulation velocity. Finally, any vertical motion other than the tidal induced motions

can contribute to P.

We will now show how to separate $-V_x$ from P. ERS-1 was right looking in 1992 and Radarsat-1 was left looking during the AMM-1 Antarctic mission. As Table 1 shows, ERS-1 interferogram (3069-2940) is built in reference to the oldest amplitude image (orbit 2940), and Radarsat1 interferogram (9852-10195) is built in reference to the most recent image (orbit 10195). If we assume that Vz is the same in 92 and 97, we have in 92:

$$\phi_{92} = \frac{4\pi}{\lambda}(-V_x \sin(\psi) + V_x \cos(\psi)\tan(\alpha) + V_z \cos(\psi))\delta t_{92} \tag{4}$$

where we explicitely make the slope contribution appear, V_z is any vertical motion except that due to slope, and δt_{92} is 24 days. In 97, with Radarsat-1, we have:

$$\phi_{97} = \frac{4\pi}{\lambda}(-V_x \sin(\psi) - V_x \cos(\psi)\tan(\alpha) - V_z \cos(\psi))\,\delta t_{97} \tag{5}$$

where δt_{97} is 9 days.

Comparing equations (4) and (5), we note that the contribution $P = V_x \cot(\psi)\tan(\alpha) + V_z \cot(\psi)$ to the phase, changes signs between 92 and 97. In this transformation, we suppose to the first order that ψ is constant, which is almost the case ($\psi_{92} = 23.4°$ and $\psi_{97} = 28°$). We also consider the track directions to be the same (they differ by 9.9°). We finally assume that V_x and V_z are unchanged, at least to first order.

In Figure 5, apart from the large scale horizontal behaviour, we observe patterns along the flanks of the rift and at the tip of the rift. These patterns are better detected if we take the derivative of the signal. This is shown in Figure 6 ,which gives a view of all the rifts. In this figure, the background horizontal creep is homogeneous and the patterns around the rifts are more visible .

If we come back to Figure 5, we can notice how in 92 and 97, the patterns are opposed. This is particularly true at the tip, where in 92, the fringes can be seen to point towards the tip, whereas in 97, the fringes point outwards. As we have seen in equations (4) and (5), this type of reversal is characteristic of a vertical motion. Since the tidal perturbation near the rifts is inexistent, and since

any slope induced vertical displacement would yield a dissymetry in slope, we conclude that these patterns are due to a vertical creep, not to tide.

Figure 7a and 7c (left parts) show the vertical motion for rift 3 and 5 in 97. We have eliminated $-V_x$ by fitting on each side of the rift a linear fit to $-V_x$. This allows us to eliminate even the velocity differential spotted in Figure 3. It can be seen that in each case, two bands of positive V_z are present, as can be seen in the Figure 7b and 7d. Bands are 1 km wide and V_z reaches values of .8 ma^{-1}. In the immediate vicinity of the rifts, V_z becomes strongly negative. It is also the case at the tip of the rift: there is a concentration of negative velocity, which gives this characteristic pattern to the fringes in Figure 5.

We find the tip patterns to be similar in rifts 1,2 and 3, the most active ones. In the case of rifts 4 and 5, which are inactive, the bands of positive V_z are still present, but the tip pattern is absent. We also find bands of positive velocity at the ice front. This leads us to model this deformation as resulting from a hydrodynamic creep of the ice shelf.

4.2 Hydrodynamic creep of the ice shelf

We have seen that along the rifts and at the tip, vertical perturbations are visible. To explain those perturbations, we use a model developped by Reeh (68) to explain the calving of iceberg, which we generalize to apply to a 2-D plate. Basically, the idea is that the hydrodynamic pressure of the water on the faces of the rift bends the ice shelf along the sides of the rift, generating a vertical motion which is detected in our interferograms. For a complete explanation of the concepts, we refer the reader to Reeh (68). We present the model and the finite element implementation in detail in Appendix 1.

To validate our model, we replicated the simulation results of Reeh in one dimension and verified that we indeed obtained the same results. Figure 8a shows the evolution of a profile perpendicular to the rift. It can be seen, that perpendicular to the rift, V_z reaches a maximum about 500 m from the rift. This maximum decreases in intensity with time, and the profile translates towards the rift. This

maximum is the one responsible for the narrow bands observed along the rifts. Figure 8b shows the evolution of the maximum values with time for different viscosities,μ (Figure 8b). It can be seen that V_{zmax} decreases asymptotically with time, and that the rate of decrease is inversely proportional to μ.

The generalization of the model to a plate, allows for the interpretation of the tip patterns as well. We have conducted a static (no propagation) and dynamic modelling of the rupture. In the dynamic case, we artificially opened the mesh at the tip of the rift at each time increment. The geometric configuration of the plate we use is shown in Figure 9a.

4.2.1 Static case

To match the model with the observations, we conduct calculations with different widths e. We obtain a good fit with $e > 3000$ m.

In order to chose our model viscosity, we compute a viscosity profile from the velocity maps we have, using:

$$\sigma' = B\,\dot{\varepsilon}^{\frac{1}{3}} \tag{6}$$

where σ' is the stress deviator, $\dot{\varepsilon}$ the strain rate and B the flow constant which depends on the temperature and ice constitution. We can deduce μ (Rignot and Mac Ayeal (98)):

$$\mu = \frac{B}{2(\frac{\partial V_x}{\partial x}^2 + \frac{\partial V_y}{\partial y}^2 + \frac{1}{4}(\frac{\partial V_x}{\partial y} + \frac{\partial V_y}{\partial x}^2 + \frac{\partial V_x}{\partial x}\frac{\partial V_y}{\partial y})^{\frac{1}{3}})} \tag{7}$$

For B, we use $B = 2.1\ 10^8$ Pa $s^{-\frac{1}{3}}$. The viscosities obtained from the observations are in the range 10^{13} to 10^{15} Pa s, with the largest values recorded far from the rifts and the smaller ones near the rifts. If we input the observed viscosity profile in our model, we find that the results remain the same if we chose a constant model viscosity $\mu = 10^{14}$ Pa s.

Another way of chosing the model viscosity is by computing the evolution of V_{zmax} in time, for different viscosities (Figure 8b). We superimpose these curves with the observed values of V_{zmax} for

the different rifts. The age of each rift is estimated from the distance to Hemmen Ice Rise and the mean ice shelf velocity. The best fit is obtained for $\mu = 10^{14}$ Pa s. Note that rift 4 deforms more rapidly. We will explain this in the discussion.

In either case, $\mu = 10^{14}$ Pa s proves to be the best value for the model viscosity. We show the results of the computation together with the vertical velocity map in 1997 for rift 5, in Figure 7a. Figure 7b also shows a comparison between the observations and the model on three profiles taken perpendicular to the rift. We use the following input data: $\mu = 10^{14}$ Pa s, $L = 30$ km, $2e = 12$ km, $\rho_{water} = 1023$ kg m^{-3}, $\rho_{ice} = 917$ kg m^{-3}and $h = 500$ m where L is the length of the plate, $2e$ the width, ρ_{water} the water density, ρ_{ice} the ice density and h the ice thickness. We carry the computation over a period of 40 years.

Figure 7a and 7b show a good fit between observations and model. The tip deformation pattern is absent in the two cases, which confirms that rift 5 is not propagating. We had seen it was the case in Table 2 from the observed propagation rates. Near the edges of the rift, our model predicts that V_z becomes strongly negative. In the observations,however this cannot be assessed because we do not have a reliable signal in this area. Nevertheless, the observed V_z decreases near the edges, which is consistent with the model.

4.2.2 Dynamic case

In the dynamic model, the crack is artificially opened. At each time increment, we open one cell of the mesh in front of the rift. The value of μ and the size of the cell determine the propagation rate of the rift. The results are shown in Figure 7c and 7d, together with the observations for rift 3 in 97. As for rift 5, we show the velocity map and the profiles. The propagation rate in the model is 300 ma^{-1}.

Rift 3 exhibits the same V_z positive bands along the rift, but the deformation at the tip is different. If we compare the observations in Figure 7a and 7c, we see that a wide pattern develops. The positive bands (yellow) circle around the tip and a strong negative singularity (blue) develops at the tip. The

model accounts well for these modifications, which suggests that the tip pattern modification is characteristic of an actively propagating rift.

Some discrepancies between the model and the observations appear in profile 3 of Figure 7d. The magnitude of V_z is too large in the model, near the tip of the rift. We have checked that this discrepancy is not due to the choice of μ. We attribute it to the simplification of our generalized viscous plate model. To evaluate the propagation rates of rifts from the magnitude of tip deformation patterns is therefore a difficult problem, and we have not made any attempt to pursue this aspect of the study.

We have taken care to open the mesh at each time increment, which means that the rupture process in our model is continuous. The good fit between the model and the observations is a strong indicator that this hypothese is correct. This is of great importance for the application of Linear Elastic Fracture Mechanics discussed next.

5 Elastic fracture singularity

We have seen in the previous paragraph that the tip pattern can be interpreted as a vertical hydrodynamic creep of the ice shelf. We now verify that this pattern is not influenced by the concentration of stress predicted by the Linear Elastic Fracture Mechanics, which could lead to a horizontal velocity pattern as the rift opens. As can be seen on Figure 6, the ice shelf has an almost uniform positive strain rate, which leads to an opening of the rifts with a mode I fracture (Anderson p53).

LEFM predicts the displacement jump across a rift in mode I to be (Hellan p237):

$$\Delta u = \frac{K_I}{G}\sqrt{\frac{r}{2\pi}}\frac{4}{1+\nu}$$

where r and θ are polar coordinates, Δu the displacement jump (figure 9b), K_I is the stress intensity factor and G is the shear modulus of ice.

The rift is propagating at a rate $v = \frac{\partial r}{\partial t}$, we have:

$$\Delta v = 2\frac{K_I}{E}\frac{v}{\sqrt{2\pi r}}$$

where E is the young modulus.If we use $K_I = .2$ MPa $m^{-1/2}$ (Mulmule and Dempsey (2000)), $v = 1000$ ma^{-1} and E=9 10^9 Pa (Petrenko p39), we get:

$$\Delta v = \frac{5.6\ 10^{-10}}{\sqrt{r}}$$

In order to observe such a signal with INSAR, Δv should be at least .1 m a^{-1}, which gives $r \leq 4$ cm. This is much less than the resolution cell (7m) of the radar, so the singularity is not observable in our interferograms.

Nevertheless, as shown by Mulmule and Dempsey (2000), the behaviour of large cracks in tabular ice plates of size ≥ 200 m should be well explained by LEFM. On a large scale, we can assume that the ice shelf behaves like a cracked rigid body in translation, and predict the propagation rate of rifts. Propagation is assumed to be continuous and the shelf to behave like a double cantilevered beam of thickness h submitted to a constant stress on the flanks of the rift. Figure 9b shows the geometry used for this modelling.

The displacement jump Δu is (efunda 2002):

$$\Delta u(x) = h\,\sigma\,\frac{x^2\,(6\,a^2 - 4\,ax + x^2)}{12\,E\,I} \tag{8}$$

where Δu is the distance between the two flanks of a rift, at distance x from the tip. I is the moment of inertia of the beam ($I = h\,e^3/12$), e is the distance between two rifts. Following the LEFM, the action of external forces on a rift can be reduced to the action of a stress σ on the flanks of the rift (Andersen p66.). We will work under the assumption that σ is constant.

We calculate the strain energy due do this repartition of stress on the flank of the rift:

$$U = \frac{\sigma^2 h^2}{2EI}\frac{a^5}{5} \tag{9}$$

The driving force ϕ is derived from (Andersen p43.):

$$\phi = \frac{1}{h}\left(\frac{\partial U}{\partial a}\right)_{\sigma} \tag{10}$$

which yields:

$$\phi = \frac{\sigma^2 h}{EI} a^4 \tag{11}$$

In order to eliminate σ which is unknown, we use equation (8) at $x = a$, and we obtain:

$$\phi = \frac{\alpha \Delta u(a)^2}{a^4} \tag{12}$$

where $\alpha = 4EI/h$.

At the rupture point, we have $\phi = R$ where R is the resistance of the ice shelf. Therefore, if we derivate the equation $\phi = R$ in time, we obtain:

$$v = \frac{da}{dt} \tag{13}$$

$$= \frac{\dot{\Delta u(a)}}{\Delta u(a)} \frac{1}{(\frac{2}{a} + \frac{1}{2R}\frac{dR}{da})} \tag{14}$$

We make another hypothesis which is that the resistance $R(a)$ is constant and independent of a, ie brittle fracture. In this case, we have

$$v = \frac{\dot{\Delta u(a)}}{\Delta u(a)} \frac{a}{2} \tag{15}$$

If we make the hypothesis that the rupture is at the limit of instability, we have:

$$\phi = R \tag{16}$$

$$\frac{d\phi}{da} = \frac{dR}{da} \tag{17}$$

We then have the following result:

$$v = \frac{\Delta \dot{u}(a)}{\Delta u(a)} \frac{a}{4} \tag{18}$$

The two formulas (15) and (18) can be easily confronted to the velocity maps we have. We can evaluate the quantity $(\frac{\Delta \dot{u}}{\Delta u} \frac{a}{2})$ at the end of the rift near HIR, as determined in Figure 3b, and predict a propagation rate for the rift.

Figure 10 shows the results. We plotted the observed positions of rifts 1,2 and 3 between 1992 and 1998 and the modeled positions with propagation rates evaluated from the velocity maps in 1992 and 1997 using equation (15). The propagation is overestimated with the rate evaluated in 92, which suggests the ice shelf was unstable at that time. The fit is good with the propagation rate evaluated in 97, which suggests a stable propagation.

6 Discussion and Conclusions

The conclusions of this article are based on observations of vertical creep velocities that are three orders of magnitude smaller than the horizontal creep velocities. In order to observe the corresponding patterns, we had to choose long time spans between multiple INSAR passes (ERS-1 9 days, Radarsat 24 days). Therefore, the quality of the interferograms had to be excellent in order for the observations to be possible.

In the case of Ronne Ice Shelf, we managed to observe with a good precision the tidal oscillations, and concluded that an elastic fracture in mode III is unlikely. Yet the fatigue associated with long term tidal oscillations (22000 cycles in 30 years) could play an important role in the propagation of rifts, which we have not yet been able to explore.

The observed vertical creep is explained by a viscous plate model. This model has simplifying assumptions which must be discussed here. The main assumption is that the ice shelf behaves like a plate. At the tip of the rift and near the edges, this hypothesis not evident. Neither the temperature

variations nor the non linear caracter of the viscosity are taken into account, a nd the influence of the calving process has not been considered: we work under the hypothesis that the edges of the rifts do not calve. But as Reeh showed in his study, the surface strain produced by a bending of the ice shelf is at the origin of the calving of icebergs. The anomaly spotted in Figure 8b for rift 4 could be due to calving events that increased the vertical velocity. This could also be the main reason for the presence of debris ice in the rifts discussed by Rignot and Mac Ayeal (1998). Taking into account this calving process could lead to an increase in the predicted vertical velocity, or a decrease in the viscosity used to model the observations.

The precise evaluation of propagation rates of the rifts from the tip deformation patterns is a difficult problem. The differences between model and observations in Figure 7d (profile 3) show that linking V_{zmax} at the tip of the rift to the propagation rate is difficult. One last observation previously made by Reeh (68) is the absence of undulations predicted by the model in the data. Figure 8a shows that at a distance of 4 thicknesses, the model predicts a second peak of vertical velocity. This is not observed in the velocity maps, even on the older rifts. This inconsistency has yet to be resolved.

Despite these limitations, the tip pattern is well explained by the viscous model, which suggests that the propagation of rifts is a continuous process. The instability of the rifts will result from an evolution of the resistance $R(a)$, as discussed in last section. This instability can be forecasted from the dynamic and geometrical properties of the ice shelf. A key factor is the driving stress applied to the rift. By modelling the rift as a cracked double cantilevered beam, we made a strong assumption on the nature of the driving force but this assumption yields results of the same order of magnitude as the observed propagation rates.

The difference between predicted and observed velocities can be explained by the non brittle character of the rupture or by the instability of the propagation. In order to get more precise results, the resistance $R(a)$ and the origin of the driving force ϕ must be evaluated, which necessitates more interferograms at different times.

7 Acknowledgements

This work was performed at the Jet Propulsion Laboratory, California Institute of Technology, under a contract with the National Aeronautics and Space Administration, Cryospheric Sciences Program. We thank the European Space Agency, the VECTRA project and Alaska SAR Facility for distributing the radar data employed in this study. We also thank Marjorie Schmetlz for her help in the images processing and the finite element modelling.

8 Appendix: vertical hydrodynamic creep model

8.1 Modelling

We will only show here the modifications used to generalise the Reeh 1D viscous beam model to a 2D viscous plate model. The geometry used for the modelisation is shown in Figure 9a The dimensions of the plate model are chosen in order to correspond to the rift 3 configuration.

We begin with the well known equations of a floating plate:

$$\frac{\partial M_x}{\partial x} + \frac{\partial M_{xy}}{\partial y} - Q_x = 0 \tag{19}$$

$$\frac{\partial M_{xy}}{\partial x} + \frac{\partial M_y}{\partial y} - Q_y = 0 \tag{20}$$

$$\frac{\partial Q_x}{\partial x} + \frac{\partial Q_y}{\partial y} + \rho_w g Z = 0 \tag{21}$$

where M_x, M_y, M_{xy} are the hydrodynamic moments over a section of the ice shelf, Z is the elevation of the ice shelf, Q_x, Q_y are the vertical shear forces, ρ_w is the density of the water and g the gravity acceleration. Derivating equations (19) and (20) and using (21) gives:

$$\frac{\partial^2 M_x}{\partial x^2} + 2\frac{\partial^2 M_{xy}}{\partial x \partial y} + \frac{\partial^2 M_y}{\partial y^2} + \rho_w g Z = 0 \tag{22}$$

We choose a viscous model, because the characteristic times of the phenomena observed are on the order of one year. In this case, we have the following links between elevation Z and the hydrodynamic moments:

$$\frac{\partial}{\partial t}\frac{\partial^2 Z}{\partial x^2} = \frac{3}{\mu h^3}\left(M_x + \frac{\rho_i g h^3}{12}\right) \tag{23}$$

$$\frac{\partial}{\partial t}\frac{\partial^2 Z}{\partial x \partial y} = \frac{3}{\mu h^3}(M_{xy}) \tag{24}$$

$$\frac{\partial}{\partial t}\frac{\partial^2 Z}{\partial y^2} = \frac{3}{\mu h^3}(M_y + \frac{\rho_i g h^3}{12}) \tag{25}$$

where μ and ρ_i are the viscosity and the density of ice and h is the thickness of the ice shelf. Replacing (23),(24),(25) in (22) we obtain the ruling equation for the viscous vertical creep of an ice shelf:

$$\frac{\partial}{\partial t}\nabla^4 Z + DZ = 0 \text{ where } D = \frac{3\rho_w g}{\mu h^3} \tag{26}$$

In order to solve the problem using a Finite Element Formulation, we have to find the boundary conditions. We model rift 3 as a single independent rift. The rift is propagating across a tabular segment. On the edges of this segment, we have:

$$Z = 0 \tag{27}$$

$$\vec{\nabla} Z = 0 \tag{28}$$

We will discuss these assumptions further ahead. The crack is modelled as the reunion of two faces separated by a zero distance. This corresponds to the observations: the rifts are very sharp near their tips. On these faces, the repartition of the water pressure gives a moment that will bend the shelf.

If $\vec{m}$ and $\vec{n}$ are the normal and tangent vectors to the rift faces, we have:

$$\sigma \vec{m}\vec{m} = P_w \tag{29}$$

$$\sigma \vec{m}\vec{n} = 0 \tag{30}$$

$$\sigma \vec{m}\vec{z} = 0 \tag{31}$$

with P_w the water pressure, and σ the stress tensor.

Equation (31) gives, if we consider $\vec{m} = [m1, m2]$ and $\vec{n} = [n1, n2]$,

$$\sigma_{xz} m_1 + \sigma_{yz} m_2 = 0$$

The integration of this equation along the vertical axis, leads to:

$$Q_x m_1 + Q_y m_2 = 0$$

And if we use equations (19) and (20),

$$(\frac{\partial M_x}{\partial x} + \frac{\partial M_{xy}}{\partial y})m_1 + (\frac{\partial M_{xy}}{\partial x} + \frac{\partial M_y}{\partial y})m_2 = 0$$

which in turn gives, if we use equations (23),(24) and (25),

$$\vec{\nabla}(\nabla^2 Z).\vec{m} = 0 \tag{32}$$

Equation (29) develops into

$$(\sigma_y - \sigma_x)m_1 m_2 + (m_1^2 - m_2^2)\sigma_{xy} = 0$$

which gives after integration:

$$(M_y - M_x)m_1 m_2 + (m_1^2 - m_2^2)M_{xy} = 0 \tag{33}$$

Equation (30) develops into

$$\sigma\vec{m}.\vec{m} = \sigma_x m_1^2 + 2\sigma_{xy} m_1 m_2 + \sigma_y m_2^2 = P_w$$

after integration, we have:

$$M_x m_1^2 + 2M_{xy} m_1 m_2 + M_y m_2^2 = M_{mm}$$

where M_{mm} is the hydrodynamic moment due to the w pressure. This moment has been calculated by Reeh.

$$M_{mm} = \frac{\rho_w g h^3}{12}(-3d_i^2 + 2d_i^3 + 6(d_i - d_i^2)\frac{Z}{h})$$

where $d_i = \rho_i/\rho_w$ We therefore have:

$$M_x m_1^2 + 2M_{xy} m_1 m_2 + M_y m_2^2 = M_{mm} = \frac{\rho_w g h^3}{12}(-3d_i^2 + 2d_i^3 + 6(d_i - d_i^2)\frac{Z}{h}) \tag{34}$$

In order to have a closed formulation, equation (33) together with equation (34) are not enough. We need the third equation:

$$\frac{\partial}{\partial t}\frac{\partial^2 Z}{\partial m^2} = 0 \tag{35}$$

where $\frac{\partial}{\partial m} = \vec{\nabla} Z.\vec{m}$. This is true along the rift. In order to simplify, let us suppose the rift to be along the x axis,we then have with equations (33),(34) and (35) and equations (23),(24) and (25):

$$\frac{\partial}{\partial t}\frac{\partial^2 Z}{\partial x^2} = 0 \tag{36}$$

$$\frac{\partial}{\partial t}\frac{\partial^2 Z}{\partial y^2} = \frac{\rho_w g h^3}{12}(di - 3d_i^2 + 2d_i^3 + 6(d_i - d_i^2)\frac{Z}{h}) \tag{37}$$

at the rifts.

8.2 Finite element formulation

We use different formulations to build the finite element solution. The most appropriate is a mixed-formulation with nodal functions of first degree and triangular elements.

The time iteration is an euler implicit scheme always stable. In order to run calculations for the dynamic cases of propagation of the rifts, we open the mesh at each time increment and use different meshes or different time steps to compute solutions with different propagation rates. The results of the dynamic cases prove to be stationary after 20 to 30 time iterations.

In order to check the validity of our formulation, the numerical procedure used by Reeh to solve his problem in 1 dimension has been implemented and yields to the same results.

The scheme is stable upon refinement of the mesh and we have checked the singularity with a 30000 elements mesh in the stable case. The singularity is well accounted for even with a lesser number of elements, we therefore use 3000 elements for the dynamic case.

In the dynamic case, the mesh is artificially opened in the direction of propagation at the tip of the rift. We verified that the mesh was symmetric with respect to the x axis

REFERENCES

Anderson T.L. 1995. Fracture mechanics. Fundamentals and applications. Second Edition.

Bazant Z.P. 2002. Scaling of Sea Ice Fracture. *J. of App. Mech.*,**69**, 11-24 January.

Doake C.S.M., Corr H.F.J., Rott H., Skvarca P. Young N.W. 1998. Breakup and conditions for stability of the northern Larsen Ice Shelf, Antarctica.*Nature.*,**391** 778.

Efunda Engineering Fundamentals.
http://www.efunda.com/formulae/solid_mechanics/beams/casestudy_bc_cantilever.cfm

Giovinetto M.B. Zwally H.J. 2000. Spatial distribution of net surface accumulation on the antarctic ice sheet.*Ann. of Glaciol.*,**31** 171.

Hellan K. 1984. Introduction to fracture mechanics. Mc Graw-Hill Book Company.

Jacobs, S.S., H.H. Helmer, C.S.M. Doake, A. Jenkins and R.M. Frolich. 1992. Melting of ice shelves and the mass balance of Antarctica. *J. Glaciol.*,**38** (130), 375-387.

Joughin, I.R., Kwok, R and Fahnestock, M.A. 1998. Interferometric estimation of three-dimensional ice-flow using asending and descending passes. *IEEE Transactions on geoscience and remote sensing* .,**36** (1), January.

Mulmule S.V. and Dempsey J.P. 2000. LEFM size requirements for the fracture testing of sea ice *Int. J. Frac.* **102** 85-98.

Petrenko F.V. and Whitworth R.W. Physics of ice. 1998. Oxfort University Press.

Reeh N. 1968. On the calving of ice from floating glaciers and ice shelves. *J. Glaciol.*,**7** (50).

Rignot, E. 1996. Tidal motion, ice velocity and melt rate of Petermann Gletscher, Greenland, measured from radar interferometry. *J. Glaciol.*,**42** (142).

Rignot, E and MacAyeal, D.R. 1998. Ice-Shelf dynamics near the front of the Filchner-Ronne ice Shelf, Antarctica, revealed by SAR interferometry. *J. Glaciol.*, **44** (147) 405-417.

Sanderson, T.J.O. 1979. Equilibrium profile of ice shelves. *J. Glaciol.*, **22** (88), 435-460.

Table 1. Radar images used to study the period preceding calving of iceberg A38.

Amplitude images used to acces propagation rates of rifts		
Date	Orbit	Satellite
1992 2/16/92	3069	ERS1
1996 2/23/96	24098	ERS1
1997 10/17/97	10195	Radarsat1
1998 2/2/98	14574	ERS-2

Interferograms used to acces fields of horizontal and vertical velocities			
Date	Orbit	Satellite	Interferograms
1992 2/7/92	2940	ERS1	3069-2940
1992 2/16/92	3069	ERS1	Simple difference
1997 9/23/97	9852	Radarsat1	9852-10195
1997 10/17/97	10195	Radarsat1	Simple difference
1992 2/10/92	2983	Radarsat1	3026-2983-5499
1992 2/13/92	3026	Radarsat1	Double difference
1992 2/16/92	5499	Radarsat1	

Table 2. Propagation rates of rifts between 92 and 98

Period	Rate in ma^{-1}					Imprecision
	1	2	3	4	5	
2/16/92 $->$ 2/23/96	75	920	1010	0	-170	50
2/23/96 $->$ 10/17/97	3140	370	524	-90	-90	120
10/17/97 $->$ 2/2/98	1390	3480	4520	N/A	N/A	700

Figure 1: view of the area around Hemmen Ice Rise near Berkner Island, on Ronne Ice Shelf. 1a: ERS-1 amplitude radar image obtained in February 1992. Figure 1b: corresponding interferogram. Images are geocoded with the north direction indicated by an arrow. The satellite track direction and the range direction are also given. Simple arrows near the rifts show the velocity direction of the ice-shelf flow. Double arrows represent the propagation rate of rifts. Profile AB in the right panel is plotted in Figure 3a.

Figure 2: sequence of amplitude radar images during the calving of iceberg A 38 on October the 13^{th} 1998.

Figure 3: left panel (a): velocity profile across rifts 1 to 5 in 92. This profile corresponds to the Figure 1b AB profile. Each jump in velocity is marked with the corresponding rift number. Right panel (b): evolution of the velocity differential across rift 3 in 1992 and 1997 with the distance from the tip of the rift.

Figure 4: double difference interferogram built from Radarsat1 images taken in 1992. Each fringe represents a tidal elevation of 3.4 cm. Rifts are shown by arrows.

Figure 5: interferograms for rift 3 in 92 (5a) and in 97 (5b). Each fringe represents an increment in horizontal velocity of 2 ma^{-1}. The rift has changed orientation in 97 because of the general ice shelf rotation. Notice the patterns reversal between 92 and 97 along the rift and at the tip. In 92 the fringes point towards the tip and in 97, they point outwards.

Figure 6: derivate of the velocity (longitudinal strain rate) in 1992 (6a) and 1997 (6b). The strain rate is homogeneous on Ronne Ice Shelf, which allows to spot the deformations easily. A close up of the rifts 5 and 3, in 97, is presented in Figure 7.

Figure 7: close up on the velocity of rift 5 (7a and 7b) and rift 3 (7c and 7d) in 97. 7a shows the vertical velocity maps observed in 97 on the left, and on the right, the velocity maps built with the hydrodynamic creep model. The profiles 1,2 and 3 are plotted in 7b together with the corresponding model profiles. The same is done for rift 3 in 7c and 7d. Rift 3 has been artificially rotated compared to Figure 6. On rift 5 and 3, the yellow bands in the velocity maps represent a

positive peak in vertical velocity. These bands run along the rifts. Rift 5 does not propagate, and there is no deformation pattern at the tip, whereas for the propagating rift 3 (1000 ma^{-1}) a strong pattern develops at the tip. The yellow bands seem to circle around the tip and a strong negative singularity (red color) develops. These differences are well accounted for in our model.

Figure 8: one dimensional model developped by Reeh for the vertical creep of an ice front. 8a: evolution in time of a vertical velocity profile for a viscosity of 10^{14} Pa s. 8b: evolution of $V_z max$ in time, for different viscosities. These profiles are used in order to determine the viscosity of the ice shelf, by fitting to the real velocities. The vertical velocity for rift 4 presents an anomaly that could be explained by calving events. The best fit is obtained for $mu = 10^{14}$ Pa s.

Figure 9: geometric configurations used in the finite element model of hydrodynamic creep (9a) and in the LEFM double-cantilevered beam propagation model (9b). In the finite element model, we use a cracked plate configuration with $L = 30$ km, $a = 10$ km, $e = 6$ km. and a thichness $h = 500$ m. On the red boundaries, the elevation and slopes are taken nil, on the green boundary, a hydrodynamic moment is applied. In the LEFM double-cantilevered beam model, we evaluate the propagation rate using formula (20) and measuring δU,$\delta \dot{U}$ and a at the hinge zone where the rift is rotating.

Figure 10: evolution of the propagation of rifts compared with a LEFM model, based on a double-cantilevered beam configuration. 10a corresponds to rift1, 10b to rift 2 and 10c to rift 3. Two different propagation rates have been evaluated, in 92 (except for rift 1, which did not have the required double-cantilever beam configuration in 92) and 97, using formula (20). We have plotted the distance propagated by the rifts as observed in the radar images and we have superposed our predicted curves.

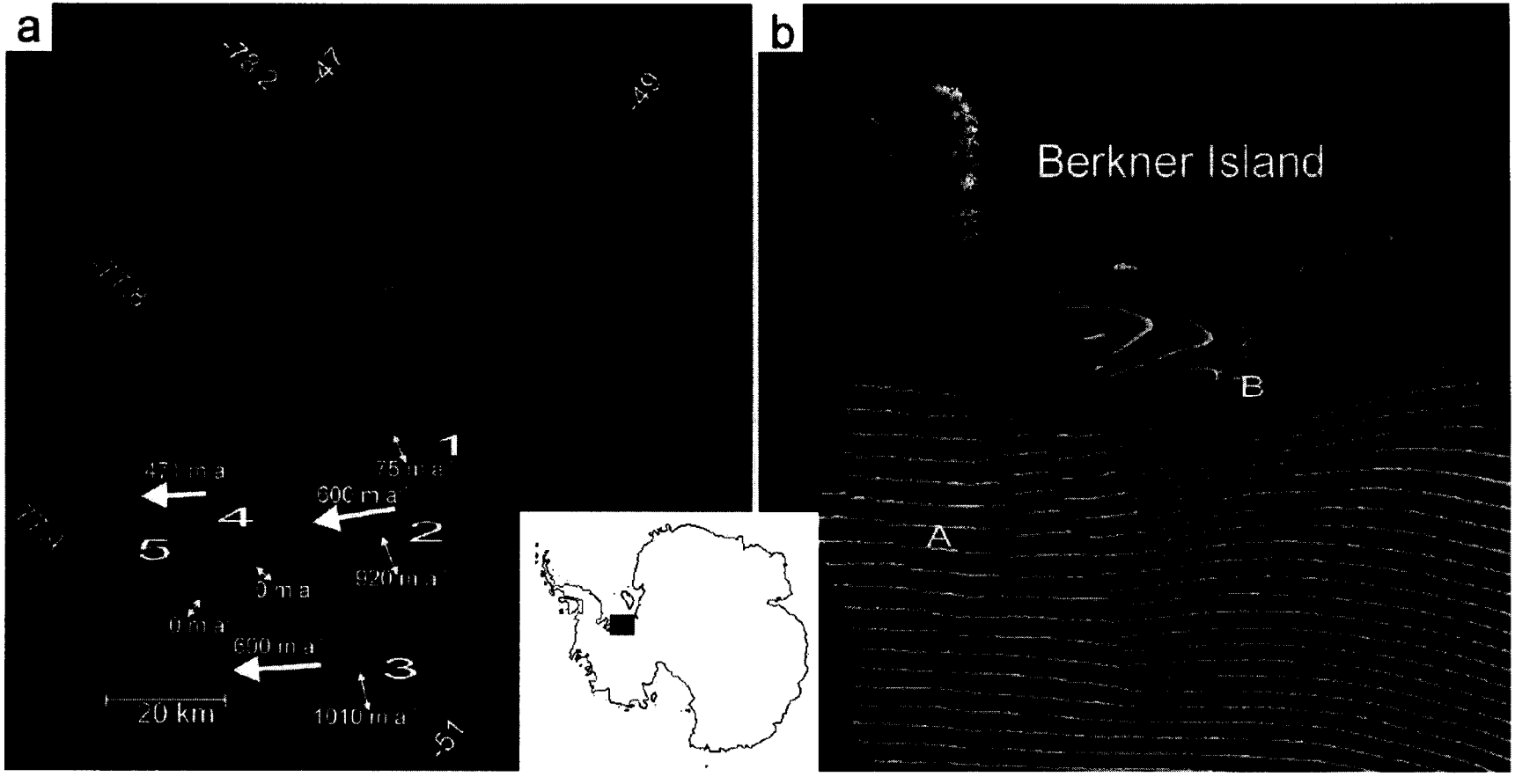
a
b
Berkner Island
A
B
1
2
3
4
5
75 m a⁻¹
600 m a⁻¹
920 m a⁻¹
690 m a⁻¹
1010 m a⁻¹
20 km

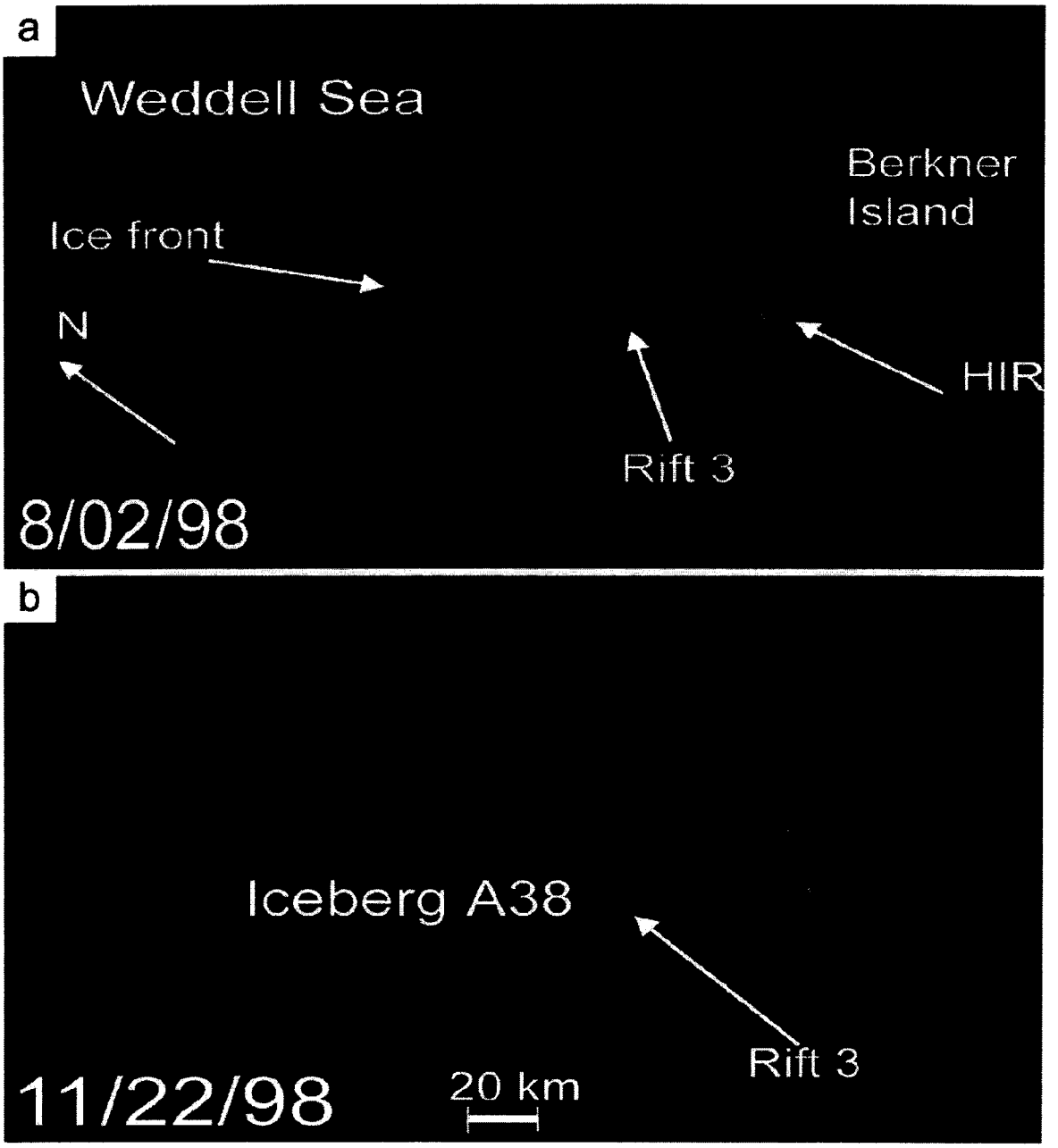
a
Weddell Sea
Berkner
Island
Ice front
N
HIR
Rift 3
8/02/98
b
Iceberg A38
Rift 3
11/22/98
20 km

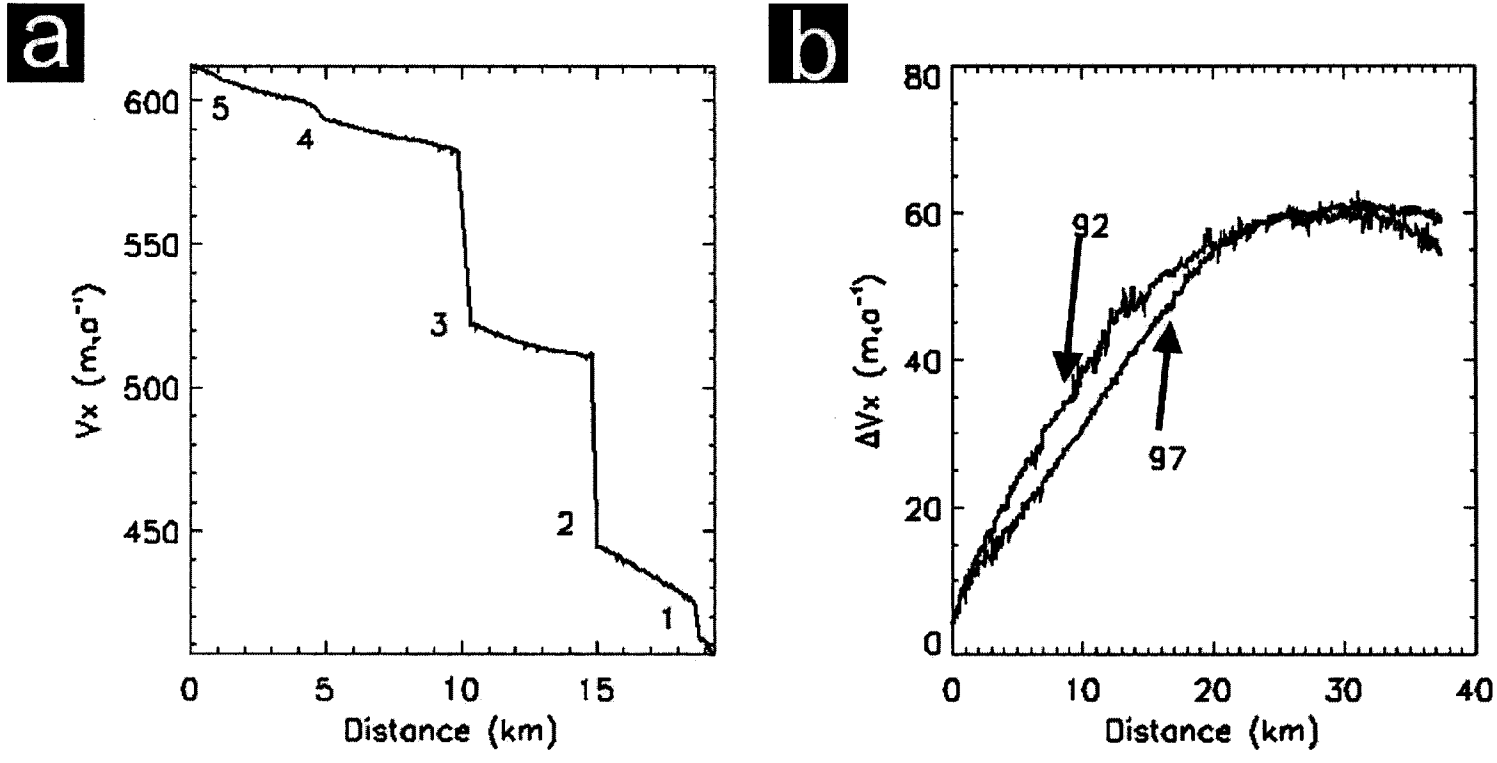
a
600
550
500
450
Vx (m.a⁻¹)
5
4
3
2
1
0
5
10
15
Distance (km)
b
80
60
40
20
0
ΔVx (m.a⁻¹)
92
97
0
10
20
30
40
Distance (km)

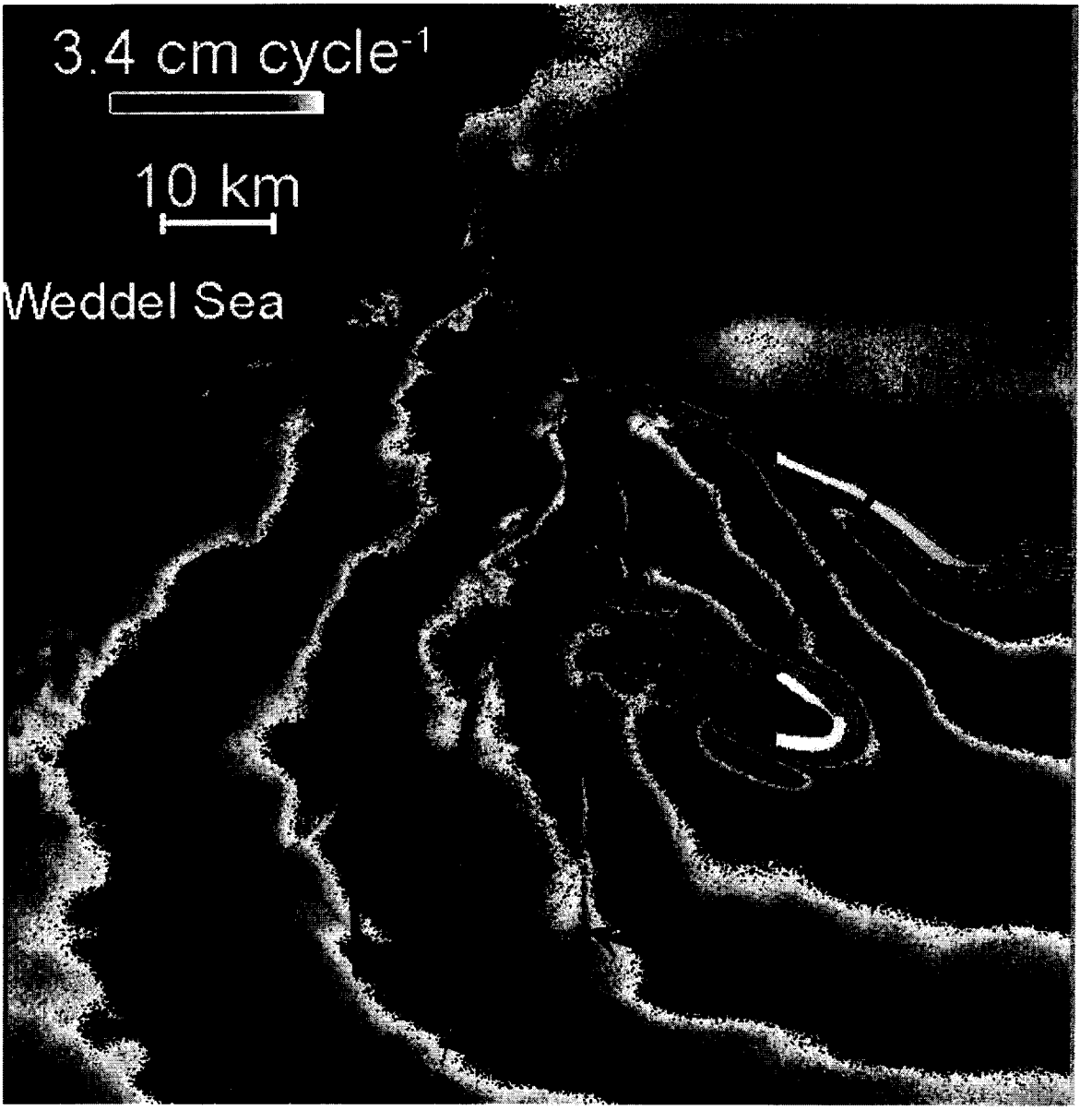
3.4 cm cycle-1
10 km
Weddel Sea

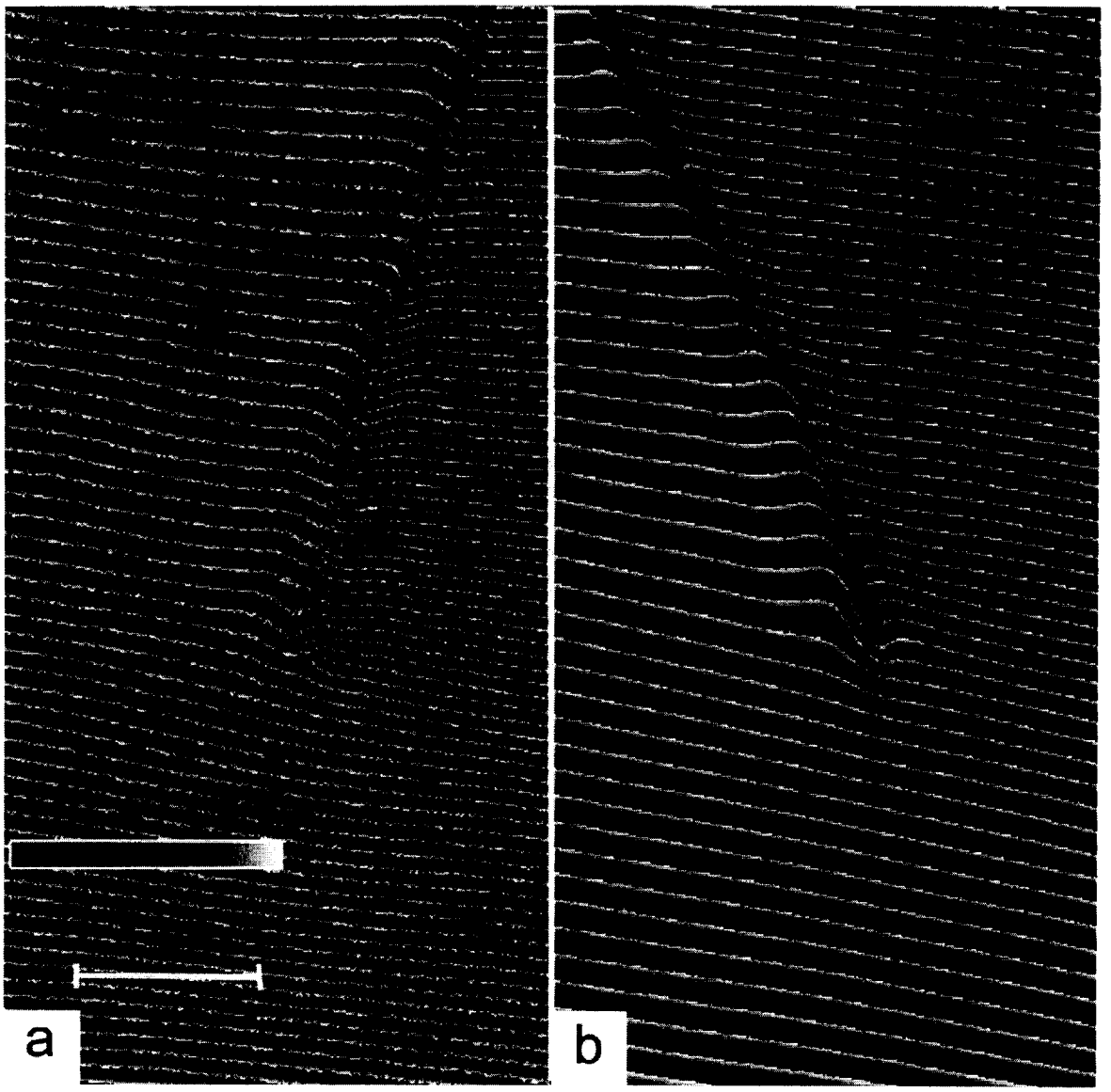
a
b

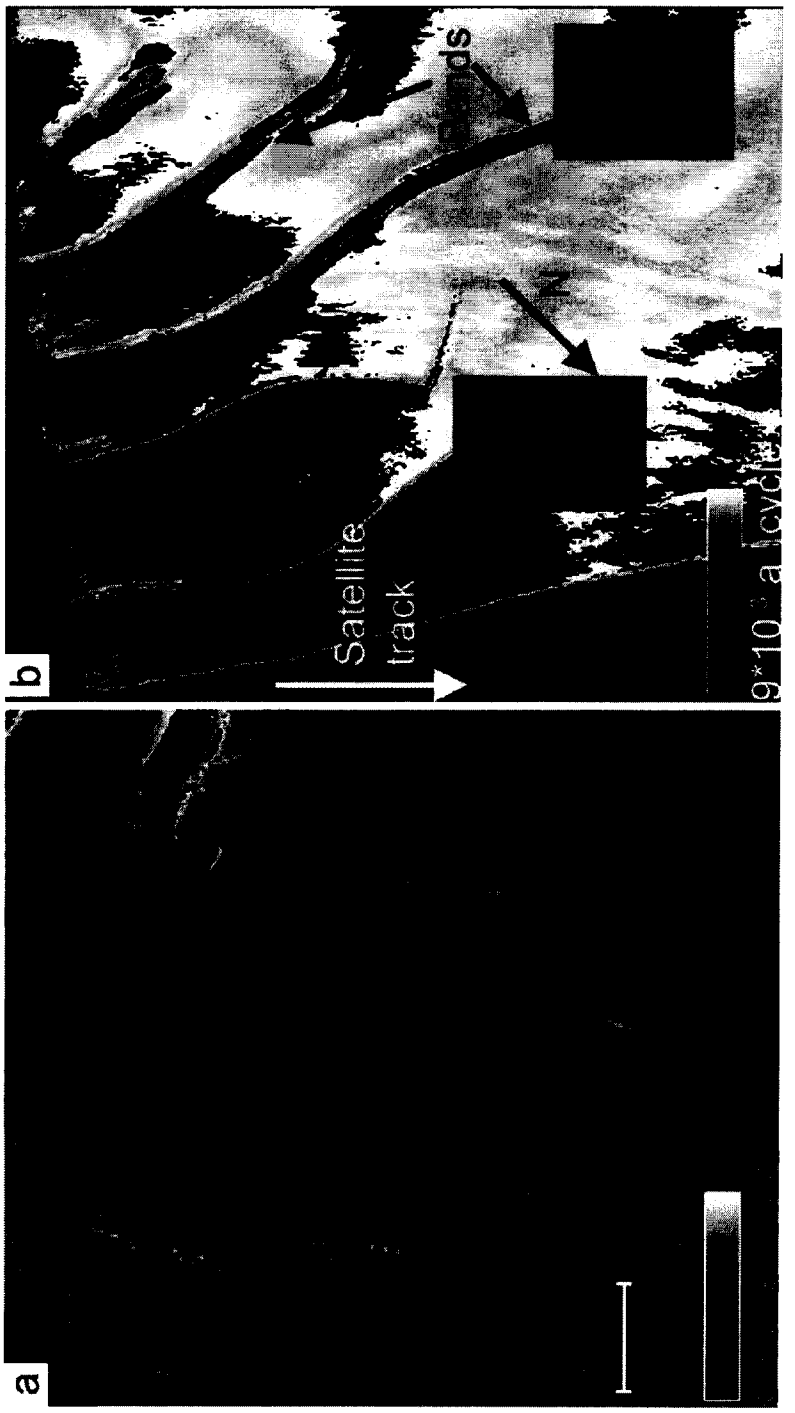
a
b
Satellite
track
ds
9*10

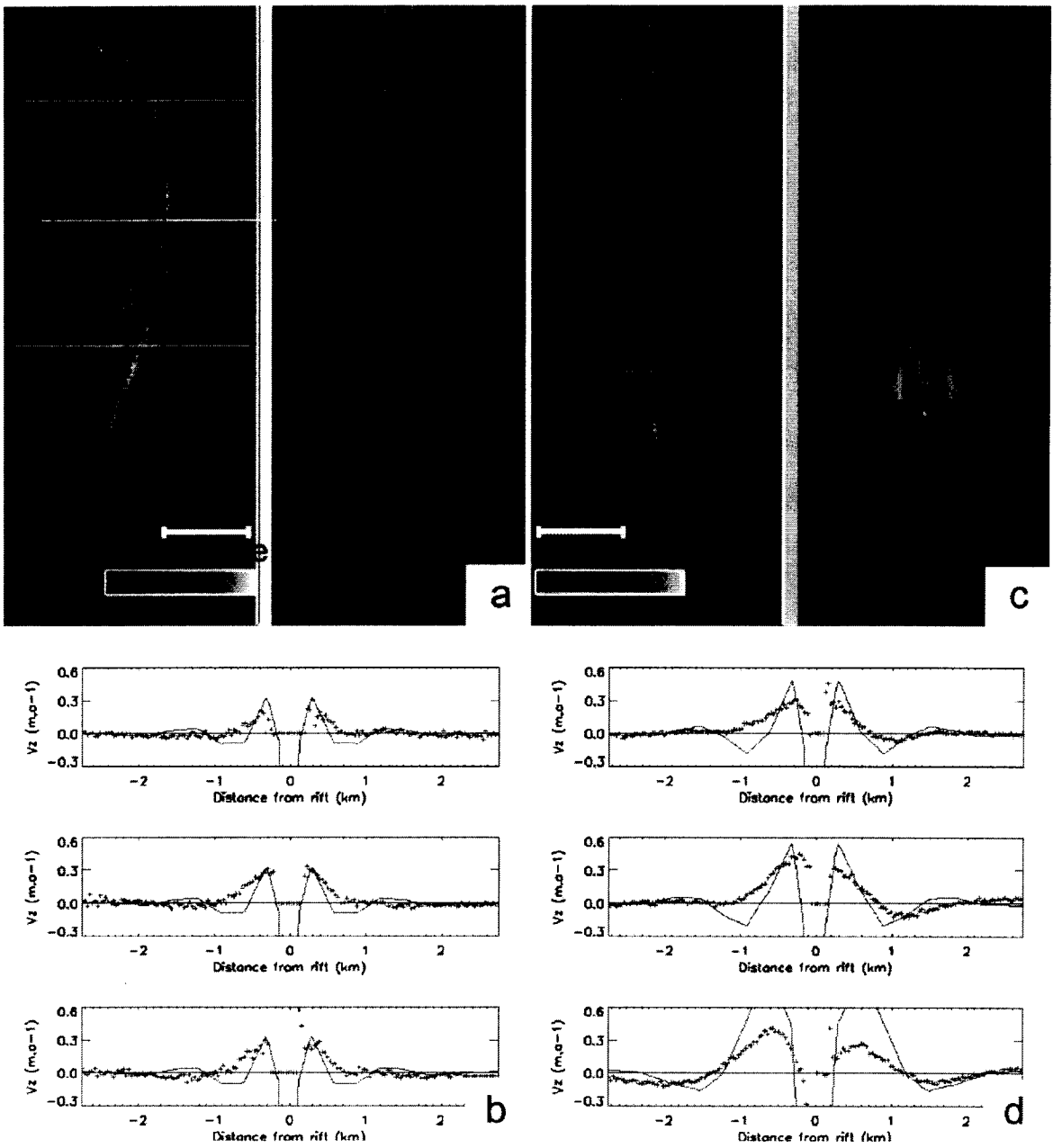
a
c
b
d
Vz (m.a-1)
Distance from rift (km)
0.6
0.3
0.0
-0.3
-2
-1
0
1
2

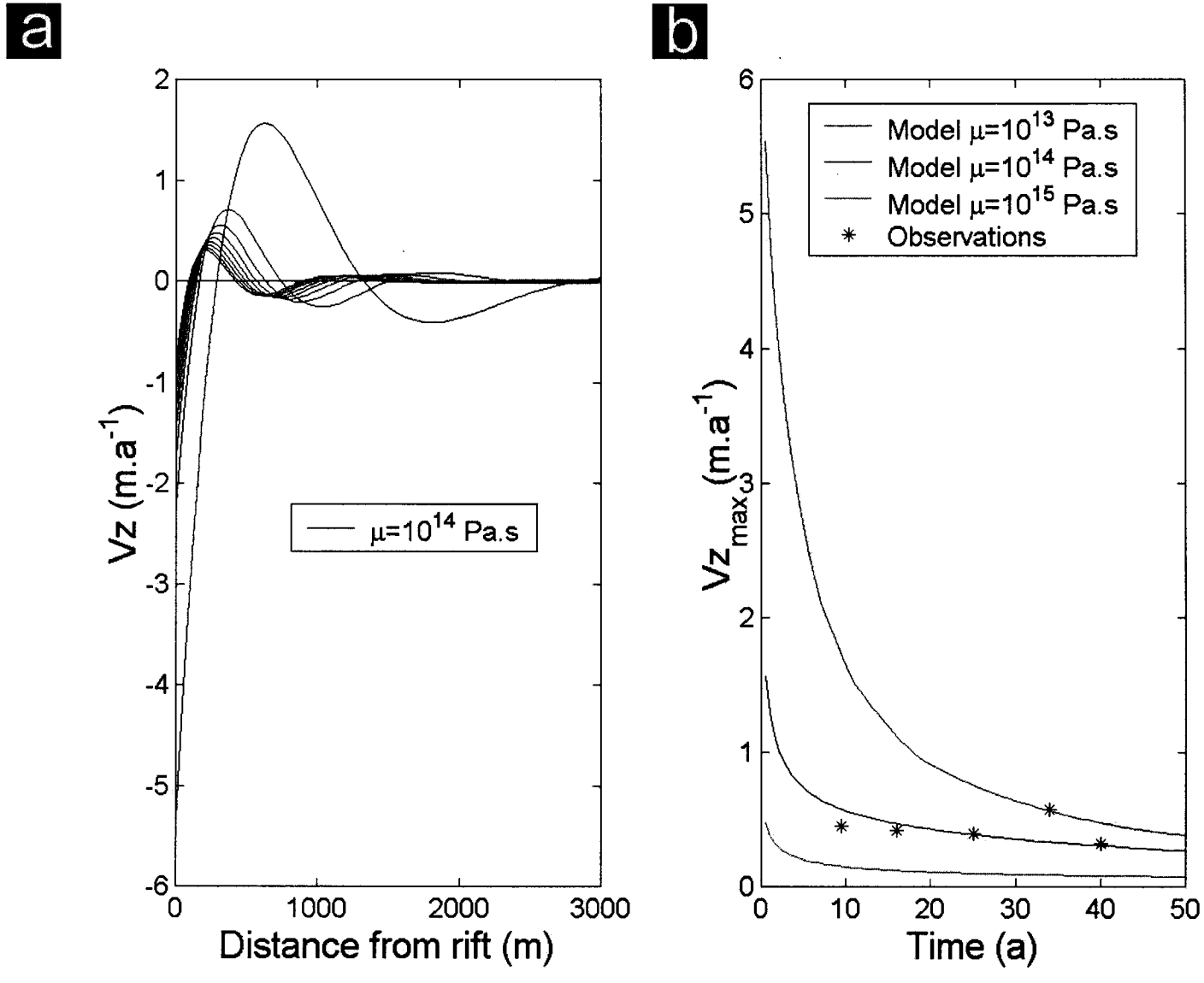
a
b
Vz (m.a-1)
Distance from rift (m)
μ=10^14 Pa.s
Vz max (m.a-1)
Time (a)
Model μ=10^13 Pa.s
Model μ=10^14 Pa.s
Model μ=10^15 Pa.s
Observations

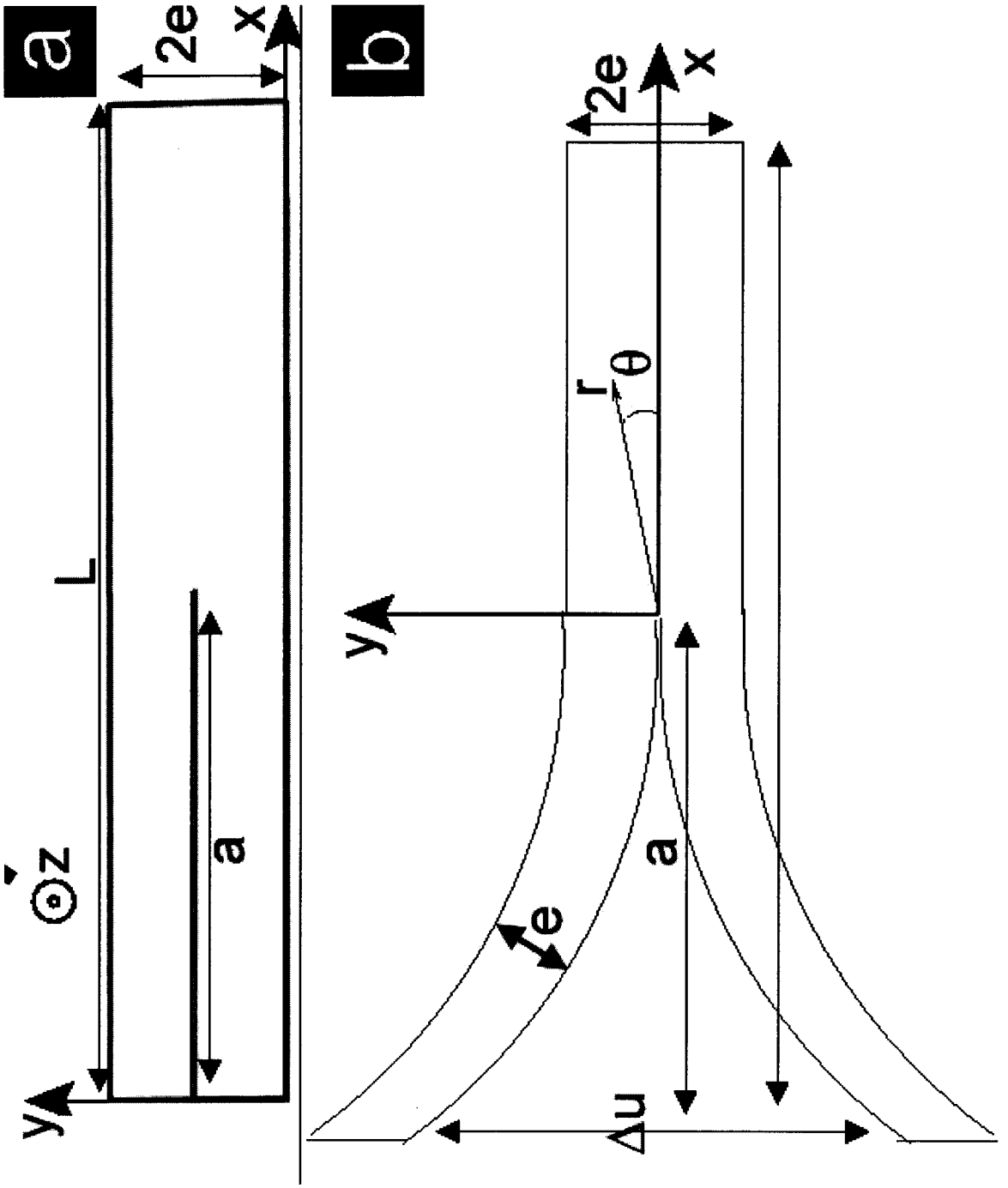
a
2e
x
L
a
z
y
b
2e
x
r
θ
y
e
a
Δu

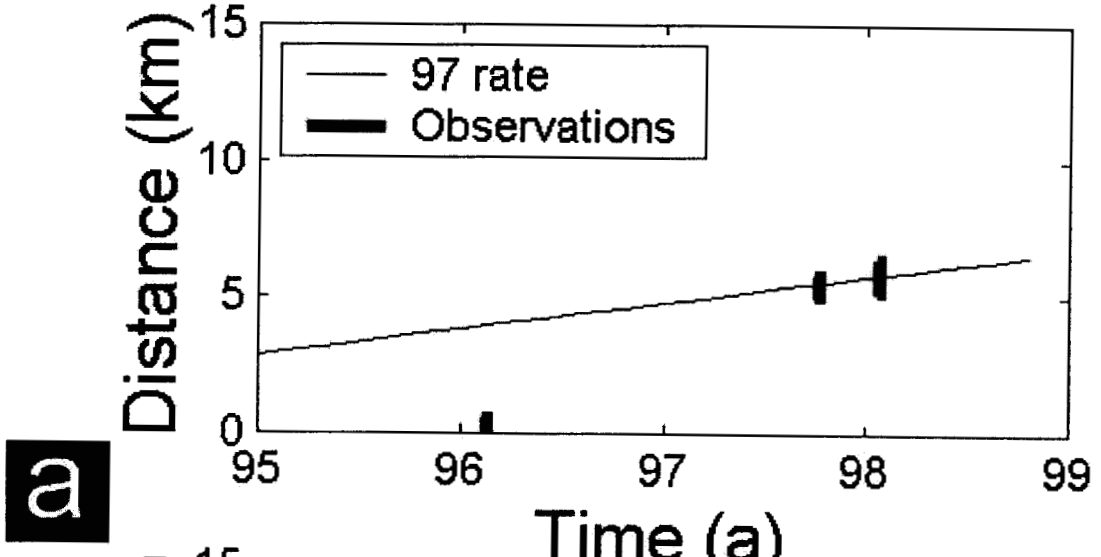
a
Distance (km)
15
10
5
0
95
96
97
98
99
Time (a)
97 rate
Observations

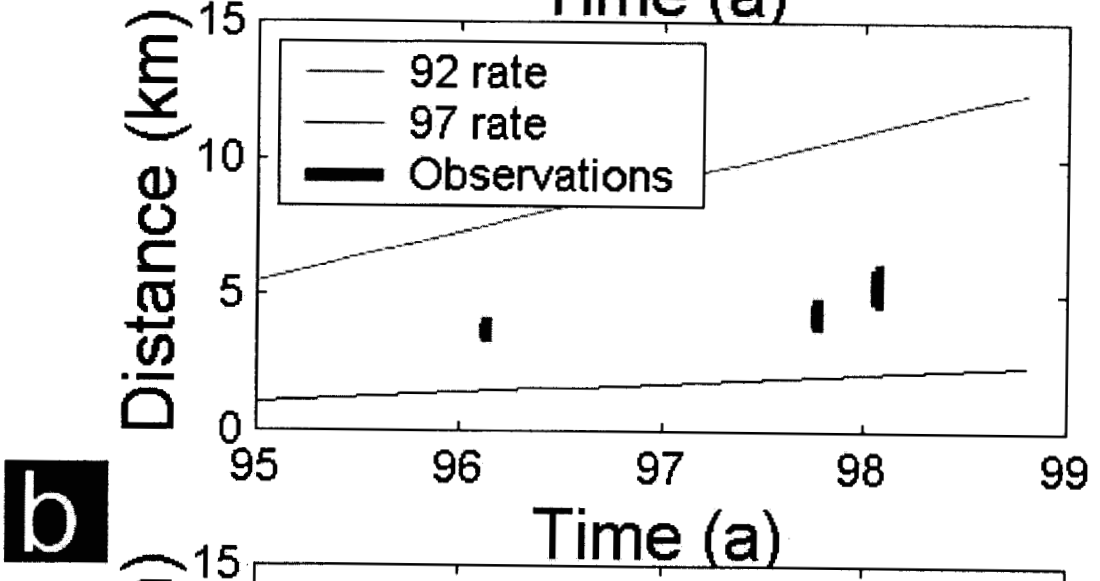
b
Distance (km)
15
10
5
0
95
96
97
98
99
Time (a)
92 rate
97 rate
Observations

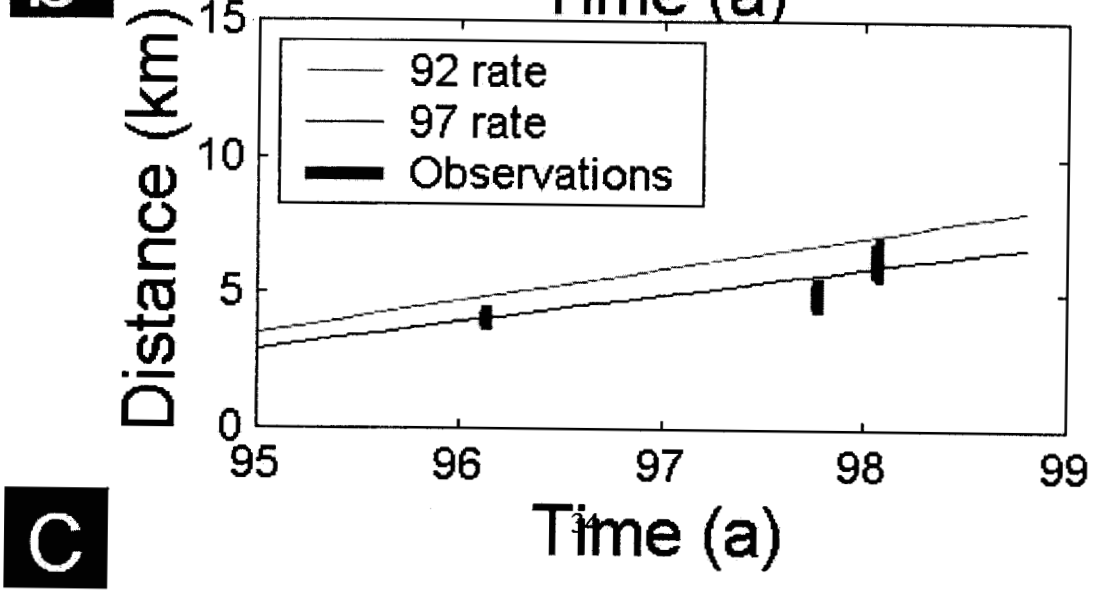
c
Distance (km)
15
10
5
0
95
96
97
98
99
Time (a)
92 rate
97 rate
Observations